POLITECNICO DI MILANO

Scuola di Ingegneria Industriale e dell'Informazione

Corso di Laurea Magistrale in Ingegneria Fisica

Dipartimento di Fisica

Non resonant inelastic X-ray scattering investigation on a carbonate glass

Supervisor

Prof. Giacomo **Ghiringhelli**

Degree thesis by

Manuel **Apollo**
matr. number 842371

Assistant supervisors

Dr. Christoph **Sahle**

Dr. Marco **Moretti**

Academic year 2016/2017

"Hunc igitur terrorem animi tenebrasque
necessest non radii solis neque lucida tela diei
discutiant, sed naturae species ratioque."

Titus Lucretius Carus
De rerum natura, Liber II

Abstract

Il carbonio ha un ruolo fondamentale per il nostro pianeta costituendo l'elemento base per la vita; inoltre i combustibili fossili, essenziali per la nostra società, sono a base di carbonio e il cambiamento climatico è regolato da questo elemento sotto forma di CO_2.

Se ad oggi la maggior parte degli studi sul ciclo terrestre hanno coinvolto il movimento di carbonio nell'atmosfera, negli oceani e nella crosta terrestre, poco si conosce delle proprietà fisiche e chimiche di questo elemento nelle profondità della terra, dove ne è contenuto più del 90% delle riserve globali sotto forma di idrocarburi e minerali. In particolare, nei fusi carbonati il carbonio può essere immagazzinato fino alle profondità alle quali si estende il mantello inferiore, nella forma di ione carbonato.

Lo scopo di questo lavoro è di studiare i fusi carbonati in condizione di interesse geofisico per chiarire l'esistenza di una transizione di fase dello ione carbonato da coordinazione ${CO_3}^{2-}$ a ${CO_4}^{4-}$ (attesa per pressioni superiori a 70 GPa) e insorgenza di network polimerizzabili.

Data la difficoltà sperimentale nello studiare direttamente il fuso in condizioni estreme di pressione e temperatura, in questa tesi verrà studiato un vetro carbonato, dimostratosi essere un buon analogo strutturale per lo studio dei fusi a temperatura ambiente. Il campione sarà inserito all'interno di una cella di diamante in modo da poter raggiungere pressioni superiori agli 80 GPa e verrà monitorata l'evoluzione della soglia K dell'ossigeno mediante scattering Raman di raggi X, una tecnica di scattering inelastico non risonante. Questa tecnica è l'unica che permette di osservare soglie di materiali leggeri che si trovano nel regime dei raggi X molli all'interno di ambienti complessi come celle di diamante, utilizzando raggi X duri altamente penetranti per misurare lo spettro di perdita di energia.

Nel presentare i risultati verranno commentate le criticità nella realizzazione dell'esperimento, i dati ottenuti e le anomalie riscontrate, con interpretazioni basate sulla fisica e altri studi su composti e tecniche analoghe. Infine sarà fornito un riassunto del lavoro svolto con una particolare attenzione alle prospettive future in questo ambito di ricerca.

Contents

List of Figures

Chapter 1

Introduction

Carbonate melts are ionic liquids consisting of carbonate $CO_3{}^{2-}$ molecular anions and metal cations (such as K^+, Mg^{2+}, Ca^{2+}) that interact principally due to coulombic interactions. Natural evidences and laboratory experiments proved their existence inside the Earth, as reported by Jones et al.[1], where they are considered important as participants in the mobility and long term storage of deep carbon, important agents of mantle metasomatism and in diamond formation; however, little is known about their physical and chemical properties at extreme conditions due to technical challenges in performing laboratory experiments at these extreme conditions. Due to the difficulties of directly studying carbonate melts at high pressures, this thesis will be focused on carbonate glasses, which are good analogues for carbonate melts as outlined by Genge and Jones[2] and demonstrated by previous vibrational studies by Seifert[3], who suggested a high level of structural similitude. For example, the parameter NBO/T (non-bridging oxygen per tetrahedral cation) does not change between the molten and the glass state; for instance in silicate glasses 4<NBO/T<2 when they involve chains, monomers and dimers.

The aim of this study is the first time investigation of structural changes in these glasses occurring at extreme conditions, where a coordination transition from $CO_3{}^{2-}$ to $CO_4{}^{4-}$ is expected, thus affecting its physical properties (Ref. Jones[1]). One way to probe these materials at high pressure condition relevant for the Earth's mantle is by means of X-ray Raman scattering spectroscopy coupled with diamond anvil cells. Using this energy loss spectroscopy, which exploits primary X-ray energies in the hard X-ray regime, one is able to explore pressure-induced electronic bonding changes even of low-Z elements of amorphous materials by probing the unoccupied density of electronic states via the generation of a photoelectron from an inner core shell. The evolution of the oxygen K-edge should ideally be followed up to some 80-90 GPa. These pressure estimates are derived from the $CO_3{}^{2-}$ to $CO_4{}^{4-}$ transition found in the crystalline counterpart at 80 GPa[4]. In this

way, changes in coordination of carbon bondings of the sample under study, a $K_2CO_3MgCO_3$ carbonate glass, can be investigated; moreover, changes in the oxygen absorption edge can be probed in order to observe if a 3-fold/4-fold transition occurs at pressures corresponding to earth's depths where it is possible to find carbon coming from subduction plates in the carbon cycle (Ref. Dasgupta et Hirschmann[5]).

Beamline ID20 at ESRF is dedicated to inelastic X-ray scattering studies and is equipped with two spectrometers, one for resonant scattering (or RIXS, resonant inelastic X-ray scattering), the other one for non-resonant scattering (NIXS). The latter is the best choice for the purposes of this experiment: the unique number of analyzer crystals inside the analyzer chambers in combination with the 2D detectors present at the beamline allow to detect the inelastic scattering signal from the oxygen K-edge (in the soft X-ray regime) of the sample under high pressure conditions, which is impossible with other techniques (*e.g.* using soft X-ray absorption spectroscopy, soft XAS, or electron energy loss spectroscopy, EELS, as probe). This particular non-resonant technique is the so-called X-ray Raman scattering (XRS). In spite of the low scattering cross section of the XRS technique, the six analyzer chambers (the ones visible in Figure 1.1) allow to cover a big portion of the solid angle, collecting enough scattered light from the sample such that the spectra, with a very good statistic, can be constructed after 5-7 hours of exposure time.

This thesis is organised as follows.

In **chapter 2** the theoretical framework which stands behind the non resonant inelastic X-ray scattering technique is presented, showing that similar information as XAS can be obtained, with the advantage of the high penetration power of hard X-rays that allow studies under extreme environments.

Chapter 3 is dedicated to the description of the tools used for our investigation, in particular the synchrotron light source and the XRS endstation of the ID20 beamline, with a further insight into the XRS technique and in the data analysis to properly acquire the relevant data for our studies.

In **chapter 4** the sample and the sample environment are presented: in particular an explanation of the preparation of the sample, its importance in the geoscience field, a description of the diamond anvil cells (DAC) used, and the explication on the way how pressure is provided and monitored on the specimen are given.

Chapter 5 presents the results obtained by the experiment with the purpose of giving an interpretation to these results.

In the end in **chapter 6** a summary and an outlook of the entire work is given.

Figure 1.1: Cover of the *Journal of Synchrotron Radiation*, March 2017.

Chapter 2

X-ray Raman scattering

2.1 Introduction

When a photon impinges on a sample, there is a finite small probability that it is inelastically scattered. Due to the small scattering cross-section of the non-resonant inelastic X-ray scattering process, this technique was benefited vastly by the advent of third generation synchrotron sources. Multiple kinds of excitations can be probed by the non-resonant inelastic X-ray scattering technique as shown in Figure 2.1, such as valence electron excitations, phonon excitations, Compton scattering and so on. The region of

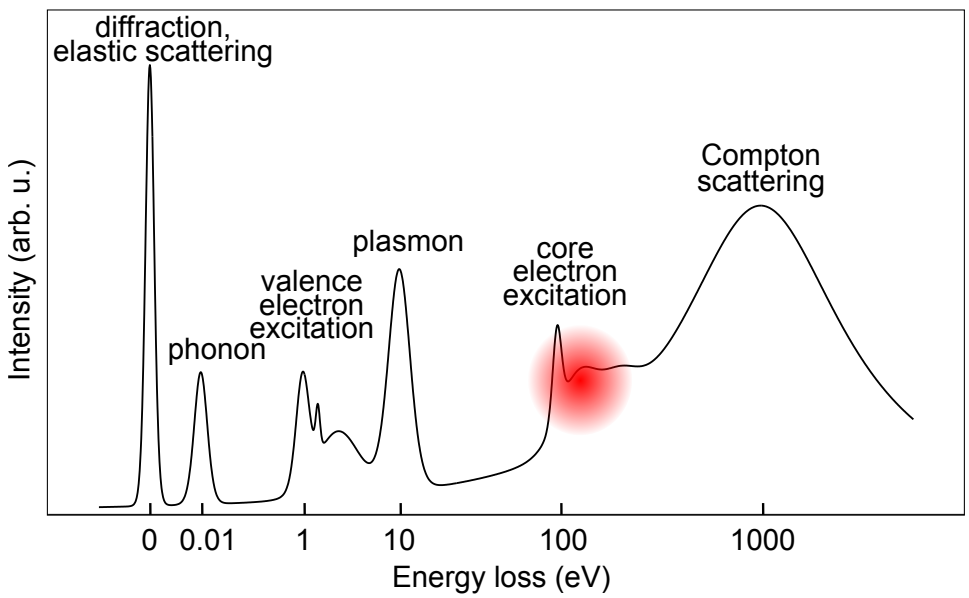

Figure 2.1: Different possible excitations depending on the energy loss. In red the energy region of our interest is highlighted. [Figure from Ref. [6]]

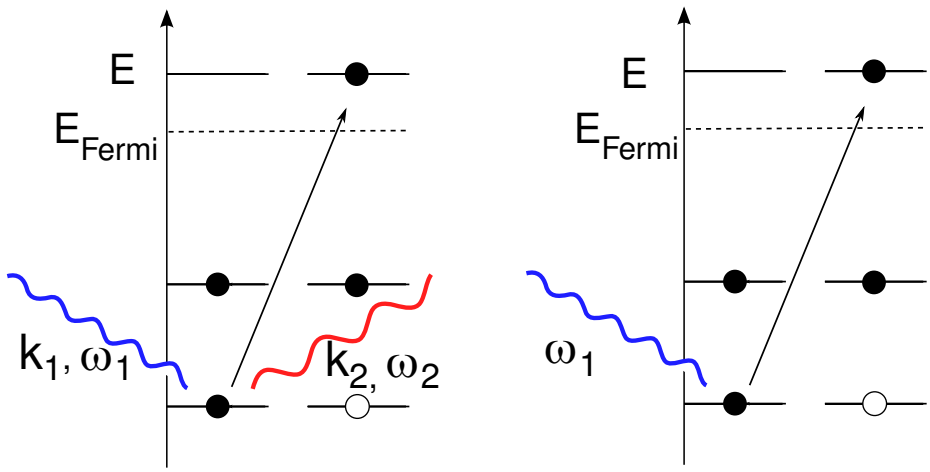

Figure 2.2: On the left, a sketch of the XRS process; on the right the XAS process.

interest for the purpose of this work is represented by the core-electron excitations, that are usually studied by means of X-ray absorption spectroscopy (XAS). The non-resonant inelastic X-ray scattering in the region of the core-electron excitation is called X-ray Raman scattering (XRS). The processes of the X-ray Raman scattering and the absorption are shown in the sketch in Figure 2.2: on the left in XRS a photon impinging on the system loses a certain quantity of energy; on the right side in XAS the photon is absorbed by the system. One of the advantages with respect to XAS is that XRS is not limited to dipolar excitations, or "the dipole selection" rules, allowing to probe also higher transitions if the momentum transfer is large (for the concept of momentum transfer see the next chapter). Moreover, as a hard X-ray technique, XRS is bulk sensitive with a penetration depth of several mm and it allows studies in extreme environments, like high pressure. This last property is the most important one in the context of this thesis. On the other hand, this technique requires long expositions (up to ten hours) because of the low count rate due to the small cross section. Besides this, the energy resolution achievable with the state of the art XRS instruments is usually worse, or comparable at most, to the typical core-hole lifetime broadenings of the often probed low Z elements' K- and L- edges.

2.2 Theoretical background

The outline of a typical inelastic scattering experiment is given by Figure 2.3. A photon of energy $\hbar\omega_1$, wavevector $\mathbf{k}_1$ and polarization vector $\mathbf{e}_1$ impinging upon a target with a state vector $|\mathrm{i}\rangle$ and energy E_i is scattered by an angle Θ into a photon energy $\hbar\omega_2$, wavevector $\mathbf{k}_2$ and polarization

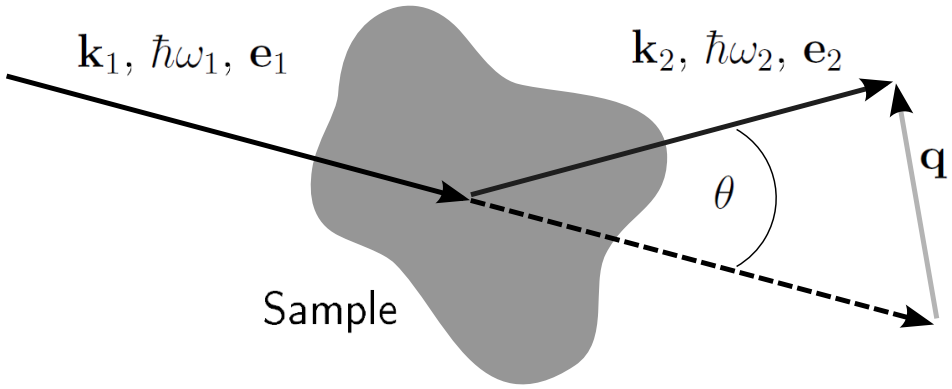

Figure 2.3: Schematic drawing of a typical inelastic scattering experiment. X-rays with wave vector $\mathbf{k}_1$, energy $\hbar\omega_1$ and polarization $\mathbf{e}_1$ are scattered by the sample into wave vector $\mathbf{k}_2$, energy $\hbar\omega_2$ and polarization $\mathbf{e}_2$ such that the energy $\hbar\omega$ = $\hbar\omega_1$ - $\hbar\omega_2$ and the momentum $\hbar\mathbf{q}$ = $\hbar\mathbf{k}_1$ - $\hbar\mathbf{k}_2$ are transferred to the scattering system

$\mathbf{e}_2$, leaving the target in a state $|f\rangle$ with energy E_f. The photon transfers an energy $\hbar\omega$ = $\hbar\omega_1$ - $\hbar\omega_2$ to the target, which also acquires a momentum $\hbar\mathbf{q}$ = $\hbar\mathbf{k}_1$ - $\hbar\mathbf{k}_2$. By the energy conservation law, it results

$$\hbar\omega = E_f - E_i \tag{2.1}$$

The modulus of the transferred momentum and the scattering angle Θ, following Schülke[7], are related by

$$q = (\omega_1^2 + \omega_2^2 - 2\omega_1\omega_2 cos\Theta)^{1/2}/c \tag{2.2}$$

if $\omega \ll \omega_1$ the last equation can be approximated by

$$q \sim 2k_1 sin(\Theta/2). \tag{2.3}$$

To realize an inelastic X-ray scattering experiment one has to produce a collimated beam of monochromatic photons, select a certain solid angle element $d\Omega_2$ of the scattered beam (thus fixing q according to 2.3), and energy analyze this part of the scattered radiation to a resolution $d\hbar\omega_2$. The measured quantity is represented by the double differential scattering cross-section (DDSCS) $d^2\sigma/$ $(d\Omega_2 d\hbar\omega_2)$, measured as a function of q and ω. It is described as

$$\frac{d^2\sigma}{d\Omega_2 d\hbar\omega_2} = \frac{\begin{array}{c} photon\ current\ into\ solid\ angle[\Omega_2, \Omega_2 + d\Omega_2] \\ and\ energies\ [\hbar\omega_2, \hbar\omega_2 + d\hbar\omega_2] \end{array}}{current\ density\ of\ the\ incident\ photons \times d\omega_2 \times d\hbar\omega_2} \tag{2.4}$$

The DDSCS can be calculated on the basis of a non-relativistic perturbation treatment by writing down the following Hamiltonian for j electrons

in an electromagnetic field, which contains the radiation field, the electrons and interaction terms

$$H = \sum_j \frac{[\mathbf{p}_j - (e/c)\mathbf{A}(\mathbf{r}_j)]^2}{2m} + \sum_{jj'} V(r_{jj'}) - \frac{e\hbar}{2mc}\sum_j \sigma_j \cdot \nabla \times \mathbf{A}(\mathbf{r}_j) \\ - \frac{e\hbar}{4m^2c^2}\sum_j \sigma_j \cdot \mathbf{E}(\mathbf{r}_j) \times [\mathbf{p}_j - (e/c)\mathbf{A}(\mathbf{r}_j)] + H_{\mathbf{R}} \tag{2.5}$$

where the summation j, j' is over all the electrons of the scattering system; $\mathbf{r}_j$ and $\mathbf{p}_j$ are the j-th electron's position and momentum operator, respectively; $\mathbf{A}(\mathbf{r})$ is the vector potential's operator of the electromagnetic wave at the position $\mathbf{r}$ of the electron, σ is the Pauli spin matrix, H_R is the Hamiltonia of the radiation field. The five terms represent in order the kinetic energy of the electrons in the presence of the photon field, the potential energy of the interacting electron system, the potential energy of the electron magnetic moment in the external magnetic field, the spin-orbit interaction and the photon field energy. Since the magnetic structure of matter is not investigated in this thesis, spin dependent terms, *i.e.* those containing explicitly the vector potential $\mathbf{A}$ and the Pauli spin matrices σ, will be omitted. Using the Coulomb gauge

$$\mathbf{E} = -\nabla\phi - \frac{1}{c}\dot{\mathbf{A}} \tag{2.6}$$

with ϕ is the Coulomb potential. In order to use (2.5) for a perturbation treatment of the scattering cross section one has to separate the interaction with the radiation part from the electron interaction part, *i.e.* to separate the terms containing explicitly $\mathbf{A}$. By doing this one obtains the components of the Hamiltonian dependent on the vector potential

$$H_{i1} = \frac{e^2}{2mc^2}\sum_j \mathbf{A}^2(\mathbf{r}_j) \tag{2.7}$$

$$H_{i2} = -\frac{e}{mc}\sum_j \mathbf{A}(\mathbf{r}_j) \cdot \mathbf{p}_j \tag{2.8}$$

the components of the electron system

$$H_0 = \sum_j \frac{1}{2m}\mathbf{p}_j^2 + \sum_{jj'} V(r_{jj'}) + \frac{e\hbar}{4m^2c^4}\sum_j (\boldsymbol{\nabla}\phi \times \mathbf{p}_j) \tag{2.9}$$

and the Hamiltonian of the radiation field, $\mathrm{H}_{\mathbf{R}}$.

Since the scattering process described is a two photon process, only the term proportional to $\mathbf{A}^2$ (*i.e.* H_{i1}) will be taken into account in the first order perturbation calculation in order to calculate the DDSCS via Fermi's golden rule (H_{i1}, which is linear in $\mathbf{A}$, does not survive first order perturbation

theory), then it follows that the transition probability per unit time for a system excited from |I⟩ to |F⟩ is

$$w = \frac{2\pi}{\hbar}|\langle F|H_{i1}|I\rangle \tag{2.10}$$

where the right hand side is proportional to $\mathbf{A}^2$; the initial state |I⟩ and the final state |F⟩ are written as products of the state vectors of the incident and the scattered photon field, with the energies

$$E_I = E_i + \hbar\omega_1; \quad E_F = E_f + \hbar\omega_2. \tag{2.11}$$

The DDSCS is obtained from the transition probability by multiplying w both by the density $\mathrm{V}/(2\pi)^3$ of states in $\mathbf{K}_2$ space and by the volume of $\mathbf{K}_2$-space which can be reached by the scattered photons in the solid angle element $\mathrm{d}\Omega_2$ and the energy element $\mathrm{d}\hbar\omega_2$ and dividing w both by the incident flux c/V and by $\mathrm{d}\Omega_2\mathrm{d}\hbar\omega_2$. Together with

$$\mathbf{K}_2^2 dK_2 = \frac{\omega_2^2}{c^3}d\omega_2 \tag{2.12}$$

one ends up with

$$\frac{d^2\sigma}{d\Omega_2 d\hbar\omega_2} = \frac{wV^2\omega_2^2}{8\hbar\pi^3c^4}. \tag{2.13}$$

Introducing the definition

$$\omega \equiv \omega_1 - \omega_2; \;\; \mathbf{q} \equiv \mathbf{K}_1 - \mathbf{K}_2 \tag{2.14}$$

and evaluating 2.13 one can write

$$\begin{aligned}\frac{d^2\sigma}{d\Omega_2 d\hbar\omega_2} = \left(\frac{e^2}{mc^2}\right)^2\left(\frac{\omega_2}{\omega_1}\right)|\mathbf{e}_1\mathbf{e}_2^*|^2\sum_{if}\sum_{jj'} g_i\langle i|exp(-i\mathbf{q}\cdot\mathbf{r}_j)|f\rangle \\ \times\langle f|exp(i\mathbf{q}\cdot\mathbf{r}_{j'})|i\rangle\delta(E_i - E_f + \hbar\omega).\end{aligned} \tag{2.15}$$

Thus the DDSCS is determined, on the one hand, by the so called Thomson differential scattering cross-section

$$\left(\frac{d\sigma}{d\Omega_2}\right)_{Th} \equiv \left(\frac{e^2}{mc^2}\right)^2\left(\frac{\omega_2}{\omega_1}\right)|\mathbf{e}_1\mathbf{e}_2^*|^2 \tag{2.16}$$

describing the strength of the photon-electron coupling and, on the other hand, by the strength of the excitation the scattering system is undergoing, expressed by the dynamic structure factor

$$S(\mathbf{q},\omega) \equiv \sum_{if}\sum_{jj'} g_i\langle i|exp(-i\mathbf{q}\cdot\mathbf{r}_j)|f\rangle \times \langle f|exp(i\mathbf{q}\cdot\mathbf{r}_{j'})|i\rangle\delta(E_i - E_f + \hbar\omega) \tag{2.17}$$

where energy conservation must be preserved. We have summed over the possible final states and averaged over all the initial states introducing the probability of the initial state g_i defined as follows

$$g_i = \frac{exp(-E_i/k_BT)}{\sum_i exp(-E_i/k_BT)} \tag{2.18}$$

where k_B is the Boltzmann constant. S($\mathbf{q}$,ω) contains all the information obtainable about the sample as an interacting many electron system by non-resonant inelastic X-ray scattering.

In the limit of small momentum transfer (*i.e.* $\mathbf{q}\cdot\mathbf{r}\ll 1$) the exponential operator can be expanded as

$$e^{-i\mathbf{q}\cdot r} = 1 - i\mathbf{q}\cdot\mathbf{r} + \frac{1}{2}(i\mathbf{q}\cdot\mathbf{r})^2 + ... \tag{2.19}$$

The second term is a dipolar operator and is the dominating term under the assumption of small momentum transfers. In this limit the dynamic structure factor is directly proportional to the photo-absorption spectrum. The first term cancels out due to the orthogonality of the eigenfunctions describing the states of the electrons involved. With large values of transferred momentum non dipolar terms can become dominant allowing transitions of non-dipolar character, such as quadrupole or octupole transitions.Within the dipole approximation, the dynamic structure factor can be rewritten in the following way

$$S(\mathbf{q},\omega) \equiv \sum_f |\langle f|\mathbf{q}\cdot\mathbf{r}|g\rangle|^2\delta(E_f - E_g + \hbar\omega_2 - \hbar\omega_1). \tag{2.20}$$

This is formally Fermi's golden rule describing an absorption process

$$T(\mathbf{q},\omega) \equiv \sum_f |\langle f|\mathbf{e}\cdot\mathbf{r}|g\rangle|^2\delta(E_f - E_g + \hbar\omega) \tag{2.21}$$

provided that the polarization vector $\mathbf{e}$ and the photon energy $\hbar\omega$ are substituted by the transfer momentum vector and the XRS energy loss. This last conclusion is crucial because it means that the same information achiavable from a XAS measurement can be obtained, as discussed also by Rehr[8]. An example of a XAS spectrum compared to a XRS one is shown in Figure 2.4.

A number of advantages in exploiting XRS technique are observed. Due to the fact that XRS is a non-resonant technique, it is possible to measure soft X-ray edges using hard X-rays. Hard X-rays are deeply penetrating and bulk sensitive, allowing to study samples under extreme conditions (in diamond anvil cell for instance), otherwise impossible to study with soft X-rays. For example, in the case studied in this thesis absorption edges of light elements such as oxygen or carbon, that are both in soft X-ray regime, need

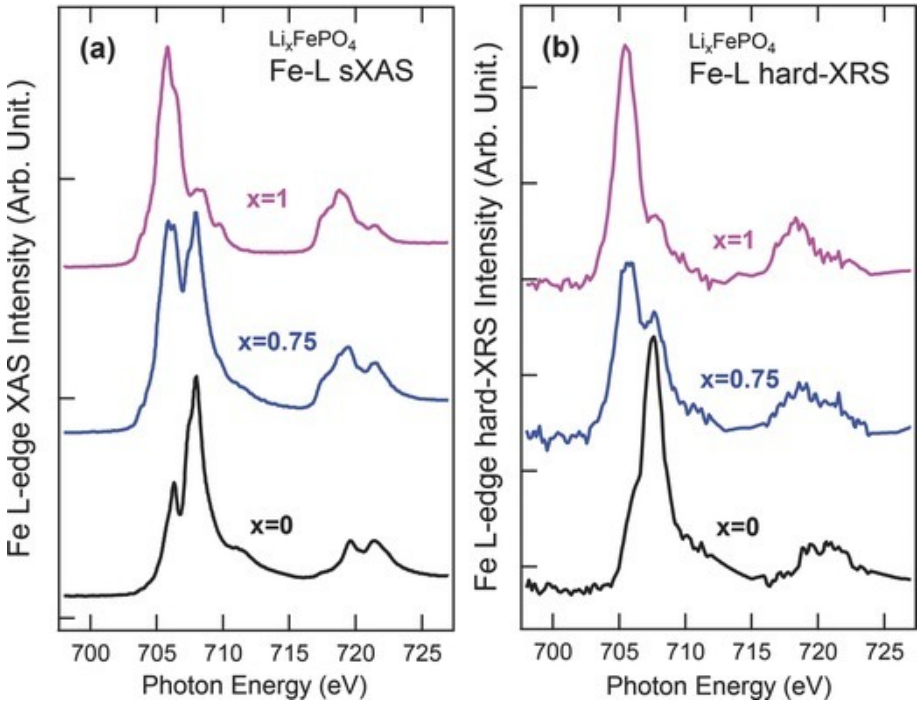

Figure 2.4: XAS vs XRS spectra. Soft XAS provides better resolution and lower noise, XRS provides bulk information [Figure from Ref.[9]]

to be detected passing through a diamond anvil cell. Non-resonant inelastic X-ray scattering is the only effective technique suitable for this purpose. On the other hand, the achievable energy resolution is not high (the overall energy resolution is at about 700 meV) and the overall count rates are low because of the low scattering cross section, indeed the counting times are in the order of several hours.

Chapter 3

Experimental setup

The experiments conducted for the realization of this thesis were performed at the European Synchrotron Radiation Facility (ESRF) in Grenoble, France, during the period of the beamtime from 2/11/2016 to 8/11/2016, at beam line ID20. This beam line, built during Phase I of the ESRF Upgrade and operational since summer 2013, is equipped with two spectrometers, one for resonant inelastic X-ray scattering (IXS) and the second one for non-resonant IXS studies of electronic properties of solids, liquids, and gases.

In the following chapter synchrotron radiation will be described; then the beamline and its X-ray Raman spectrometer will be introduced.

3.1 ESRF synchrotron radiation

In order to provide synchrotron radiation it is necessary to force charged particles at relativistic velocity to follow a circular path thanks to a magnetic field; when the trajectory changes, the electrons undergo an acceleration which results in X-rays emission. The European Synchrotron Radiation Facility (ESRF), a schematic of which is shown in Figure 3.1 [10], is a syn-

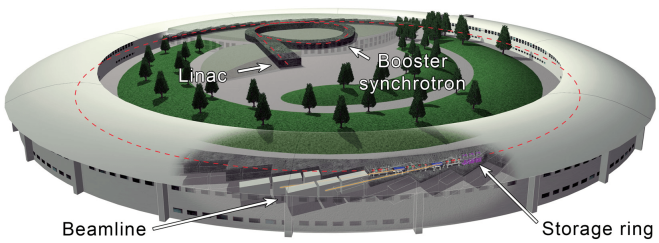

Figure 3.1: ESRF scheme, a third generation synchrontron radiation facility. Ref. [10].

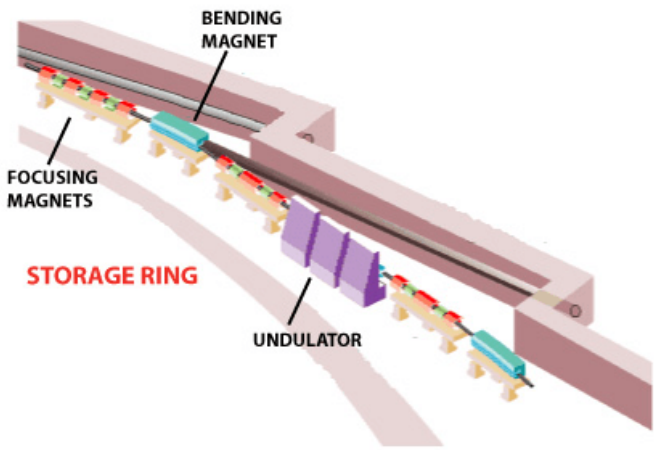

Figure 3.2: Example of a synchrotron storage ring. Ref. [10].

chrotron light source inaugurated in 1994 that works with electrons that are produced by an electron gun and linearly accelerated until an energy of 200 MeV. Subsequently, they are injected in a booster synchrotron, a circular particle accelerator 300 meter-long where the magnetic field is increased synchronously to the increasing energy of the electrons in order to make them flow in a fixed radius of curvature and to reach an energy of 6 GeV; in the end they are sent into a 844 meter-long storage ring formed by 32 straight and 32 curved sections and kept in ultra high vacuum ($\sim 10^{-9}$ mbar) in order to minimise collisions with residual particles and allowing the beam to last for many hours. Their velocity is about the speed of light, almost 300000 km/s.

The radiation can be produced, as represented in Figure 3.2, in the curved sections thanks to bending magnets or in the straight sections by the insertion devices (undulators and wigglers).

A bending magnet is a dipole magnet which generates a homogeneous magnetic field perpendicular to the plane of the storage ring inducing a Lorentz force which drives electrons onto a circular path. An insertion device is a periodic array of dipole magnets which induces a sinusoidal motion of the electron beam in the horizontal plane directly proportional to the periodicity of the magnets' spacing. In an undulator the radiation is created thanks to the inversion of magnetization in each array elements; this inversion deviates the electron path and, at each deviation, the electrons radiate. All the electromagnetic waves created interfere among themselves providing the cone-shaped X-ray beam shown in Figure 3.3 with the property to have a narrower spectral range than the bending magnet's radiation, high photon flux at particular energies (undulator harmonics) and high brilliance (an example of undulator spectra is shown in Figure 3.4).

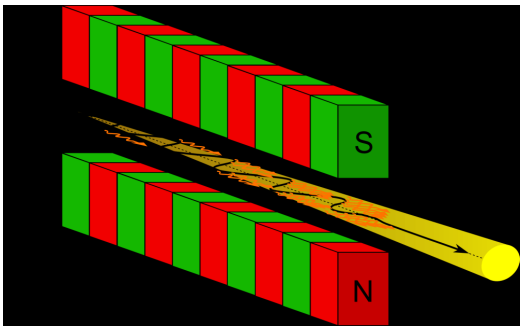

Figure 3.3: X-ray beam production by mean of an undulator. Ref. [11].

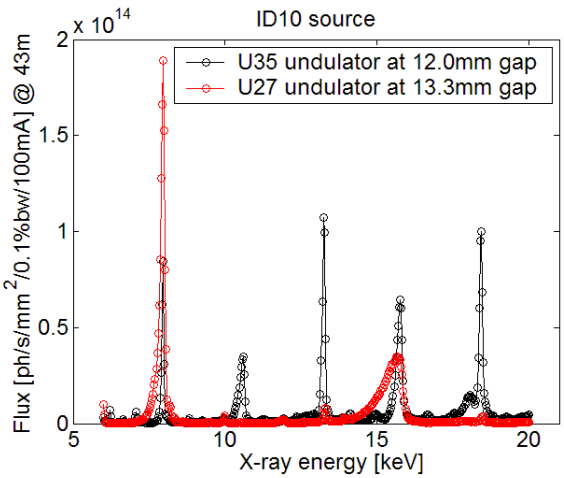

Figure 3.4: Flux spectra of the ID10 undulators in ESRF to produce 8 keV photons; higher order harmonics are visible at higher energies. Ref. [12].

The latter property is related to the spot size on the sample (in the order of μm) which is crucial where one has to study sample confined in a small diamond anvil cell, as the case of the experiment of this thesis. Tuning the gap between the magnets (io our case circa 15 mm) allows to switch between different characteristic energies.

3.2 ID20 setup

ID20 is a beamline working in the hard X-ray regime. The incident photon energies are in a range between 5 keV and 20 keV. By means of resonant and non-resonant inelastic X-ray scattering, this beamline investigates solid, liquid, and gaseous samples. A scheme of the ID20 is reported in Figure 3.5.

Four undulators in a 6 m long section with a 26 mm undulator period provide a diverging X-ray beam with a large energy bandwidth which is subsequently collected, monochromatized and focused at the sample position by the X-ray optics.

A collimating mirror (CM1) is located after the undulators: its cylindrical shape allows it to vertically collimate the beam toward the monochromator. Moreover, it is able to reduce the beam power and reject the high order harmonics from the undulator. The outgoing beam is still horizontally diverging.

After CM1, the beam reaches a Si (111) double crystal monochromator, the so called Kohzu monochromator, that is cryogenically cooled with liquid nitrogen in order to avoid damages by the beam and alterations of important parameters to keep the beam's quality stable (*e.g.* energy width, beam brightness and intensity) such as the lattice parameter: in Figure 3.6 we can see the apparatus just described. In order to select the energy one can exploit the reflection from the (111) lattice planes, by the Bragg's law [13]:

$$n\lambda = 2d\sin(\theta_{\mathrm{B}}) \tag{3.1}$$

where λ is the wavelength of the incoming photons, $d = a_{\mathrm{Si}}/\sqrt{h^2+k^2+l^2} = a_{\mathrm{Si}}/\sqrt{3}$ (where $h = k = l = 1$ are the Miller indices) is the distance between lattice planes (those with Miller index (111)), θ_{B} is the Bragg angle of the X-rays (*i. e.* the included angle between the surface and the photon beam direction) and n the diffraction order. To monochromatize the energy at a given value one could set the Bragg angle, θ_{B}, as follows:

$$\theta_{\mathrm{B}} = \arcsin\left(\frac{\lambda}{2d}\right) = \arcsin\left(\frac{hc}{2dE_i}\right) \tag{3.2}$$

where h Planck's constant, c is the speed of light in vacuum, $a_{\mathrm{Si}} = 5.43$ Å is the Si lattice parameter at 77 K, d is the lattice plane distance as defined above. Ideally the response of a perfect crystal is infinitely sharp, *i.e.* it reflects only one wavelength, according to 3.1. However, 3.1 is a simplification that neglects absorption and interference of reflected and refracted waves (Ref. [14]), and the reflected wave has an intrinsic width. For example theory of dynamical diffraction, which explains the exact shape of a diffraction peak of a perfect single crystal, yields to the so called Darwin width $\Delta\theta_{\mathrm{Dw}}$, given by:

$$\Delta\theta_{\mathrm{Dw}} = \left(\frac{\Delta E}{E}\right)\tan(\theta) \tag{3.3}$$

with $\Delta E/E$ the monochromator's energy resolution (approximately $\simeq 1.35 \cdot 10^{-4}$ for the Si(111) reflection, corresponding to $\Delta E \simeq 1.35$ eV at $E \simeq 10$ keV).

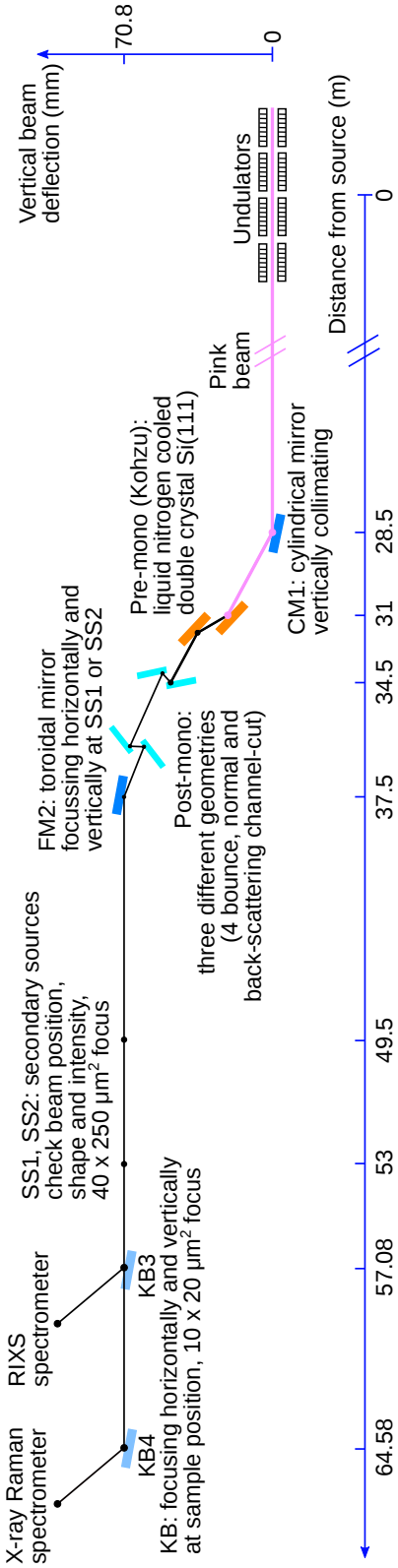

Figure 3.5: Beam line ID20 optical layout

Figure 3.6: The Kohzu monochromator with the cooling system in orange, the two Si crystals in gray. With the black arrow is represented the scattered photon beam.

For a better resolution it is possible to introduce a secondary, or post-, monochromator which, utilizing the narrower Si (311) reflection, results in an increase energy resolution of $\Delta E/E = 2.7 \cdot 10^{-5}$.

The monochromatic beam is then focused onto a secondary source using a toroidal mirror (FM2). The spot size at the secondary source is approximately 40 μm x 250 μm (vertical $\times$ horizontal). This point along the beam line serves as an optical source for the last optics element: a Kirkpatrick-Baez (KB) mirror installed at 0.75 m from the sample position which allows to have a smaller focus. This last focusing element acts in both the vertical and the horizontal direction using two elliptical mirrors. The final spot size at the sample position (which is 65 m far from the undulators) is 10 μm $\times$ 20 μm (V x H).

3.2.1 The X-ray Raman spectrometer

The Raman spectrometer installed at ID20 is dedicated to the study of shallow core electronic excitations using non-resonant inelastic X-ray scattering.

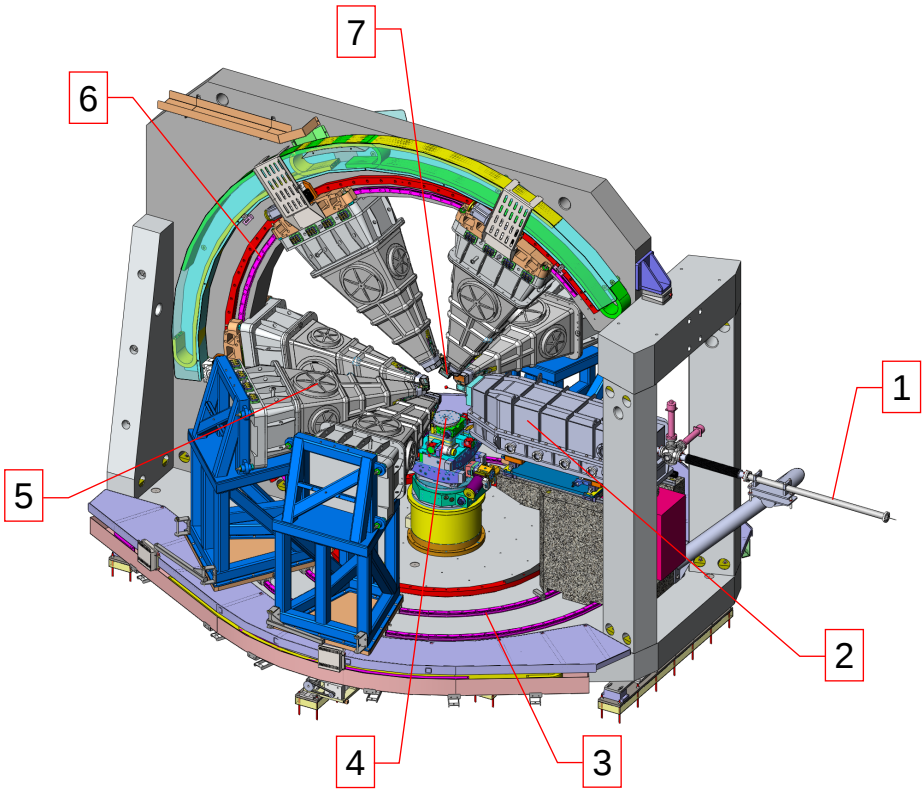

1: Incident X-ray beam
2: KB mirror
3: Horizontal rotation stage of the analyzer chambers
4: Sample goniometer
5: Analyzer chamber
6: Vertical rotation stage of the analyzer chambers
7: Maxipix detector

Figure 3.7: Schematic drawing of the X-ray Raman spectrometer.

The X-rays (coming from the right side in Figure 3.7, post 1) at about 10 KeV of energy impinge on the sample mounted on the sample goniometer (post 4 in Figure 3.7), which allows the sample to be translated x, y and z directions and rotated around these axes so that it can be centred in the beam position. Because of the small cross section of the XRS technique one needs to cover the biggest portion of solid angle possible in order to acquire the signal with enough intensity. For this reason the sample is surrounded by six modular groups (post 5 in Figure 3.7) of twelve analyzers each (as one can see in Figure 3.8) for a combined maximum flexibility and large solid angle of detection such that it is possible to simultaneously acquire different $\mathbf{q}$ values (*i.e.* the momentum transfer). Each module is equipped with a lightweight composite carbon fiber vacuum chamber at 1 mbar to minimize the absorption and the parasitic scattering from air; 10 mm long

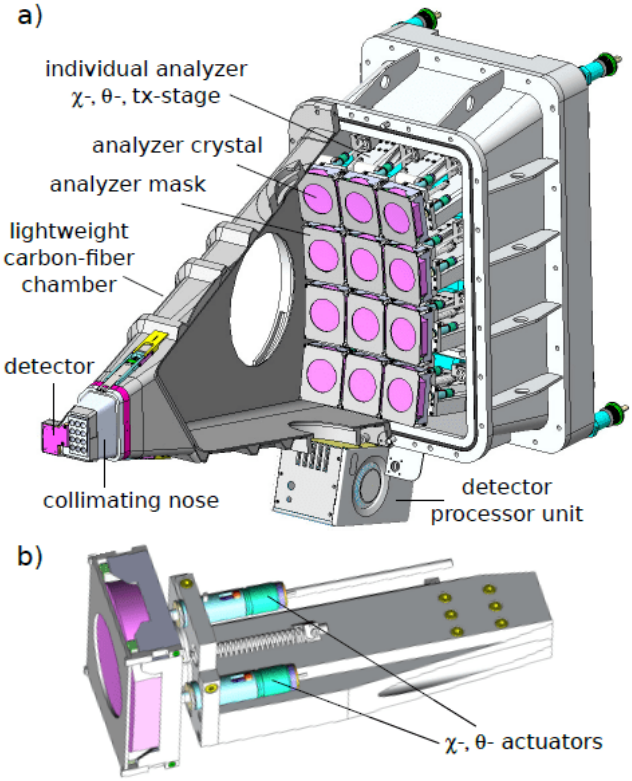

Figure 3.8: a) Modular unit hosting analyzer crystals on a 1 m Rowland circle. b) Sketch of the two rotational and one translational degrees of freedom for a single analyzer crystal.

aluminium apertures (collimating nose in Figure 3.8) are used to collimate the scattered radiation from the sample. The naming convention for the six analyzer units are vertical down (VD), vertical up (VU), horizontal left (HL) and horizontal right (HR) in the forward direction, vertical back (VB) and horizontal back (HB) in the backward direction. In the experiments the environment where the sample is placed in, a diamond anvil cell (DAC), gives geometrical constraints such that light scattered in the horizontal plane is blocked by the cell's walls and the diamonds (for more details about DAC look Chapter 4.2) such that only the vertical analyzer units were used. For the forward direction the scattering angle was set to $2\theta = 40°$ for VD, $2\theta = 80°$ for VU and for the backward direction $2\theta = 120°$ for VB allowing to simultaneously collect data at q$\simeq 3.35\mathring{A}^{-1}$, q$\simeq 6.3\mathring{A}^{-1}$ and q$\simeq 8.5\mathring{A}^{-1}$.

To achieve an energy resolution of the inelastically scattered X-rays that is in the order of the meV, the spectrometer is equipped with so-called crystal analyzers. These crystal analyzers consist of 300 μm thick single crystal Si

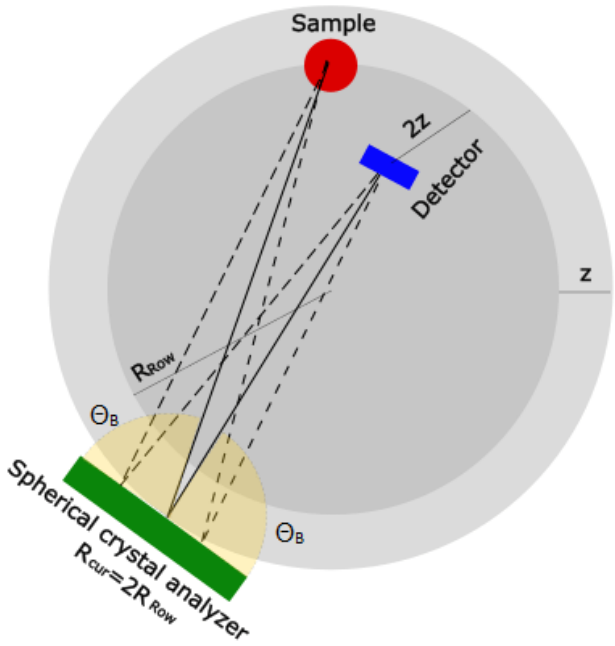

Figure 3.9: Rowland circle geometry: X-rays from the sample are diffracted by the analyzer and focused onto the detector. Sample and detector must be placed on the Rowland circle, whose radius of curvature is half of that of the crystal. If we are in backscattering geometry we have to displace the detector at a certain distnce 2z from the Rowland circle, displacing at the same time the analyzer of a z quantity in the opposite direction, adding an off-Rowland contribution. Design realized with Inkscape by the author.

wafers oriented such that the crystallographic (660) direction is parallel to the surface normal of the Si crystal. The wafers are anodically bonded to a spherical pyrex glass substrate. This procedure results in a bending radius of 1 m. However, the elastic deformation of the bending of the crystals deteriorates their properties in energy resolution, as also pointed out by Hämäläinen and others[15]. To increase the signal-to-noise ratio one could, for example, increase the size of the analyzers, but in this way there will be a decreasing in the energy resolution. Therefore, the crystals are arranged in the so called Rowland geometry (see Figure 3.9), *i.e.* all, sample, analyzer and detector are positioned on a common circle of radius R_{Row}. The bending radius of the spherical analyzer crystal is twice that of the Rowland circle. By doing so, the scattered X-rays are focused onto the detector.

To move and better focus the foci on the detector the crystal analyzers

are equipped with three motorized movements. The crystals are cut to 80 mm active diameter in one direction in order to minimize strain due to angular compression.

Thanks to the reflection provided by the analyzers, only the photons that have lost the wanted quantity of energy are then focused onto the detector positioned at the end of the chambers. The detector is a Maxipix mounted close to the sample position in order for the analyzer crystals to work in new backscattering geometry. There is one detector for each chamber; each one has 256×256 pixels, the pixel size is 55×55 μm^2.

The overall energy resolution comes from several contriubutions, such as the bandwidth of the incident beam, the bandpass of the analyzer crystal and the off-Rowland contribution (given by the configuration in Figure 3.9). This last contribution arises from the fact that the Bragg angles should be close to 90°, but a certain amount of space should be saved to the sample environment. Then the detector is placed inside the Rowland circle by a distance 2z. The Bragg angles vary across the analyzer generating a dispersion given by:

$$\frac{\Delta E}{E} = \left(\frac{zD}{R^2}\right) \cot \Theta_{\mathrm{B}} \tag{3.4}$$

where D is the size of the analyzer crystal in the dispersive direction, Θ_{B} is the Bragg angle of the analyzer reflection (like shown in Figure 3.9). The overall energy resolution is ΔE=0.7 eV as estimated from the measurement of the FWHM of the quasielastic peak of the light scattered by a piece of scotch tape put in the sample position. Attention has to be paid to spurious scattering from the sample environment, the main source of background noise.

3.3 Data analysis

In the Maxipix the data are stored as binary files, each of them contains an image of all six detectors tiled in a 3x2 manner (in the experiments discussed in this thesis only the three vertical detectors are used, for the reasons already mentioned in the previous chapter). The analyzer crystals scatter the light that is focused onto spots on the detector (12 per detector). A point source that is focused on the detector has a focus size that corresponds to the single pixel dimension (55 μm $\times$ 55 μm). The dynamic structure factor S(q,ω), as already seen in Chapter 2.2, gives the contrast for the image and thus different excitations can be chosen (electron density, valence electronic excitations or core edges). This imaging capability can be used to align the sample: if one scans, at fixed energy, the sample position through the incident beam a 2D image is created: this image represents a sample's plane in the direction of the scanning beam (see Figure 3.10 for more clarity). The spatial resolution is given by the beam size, the pixel size and the focus

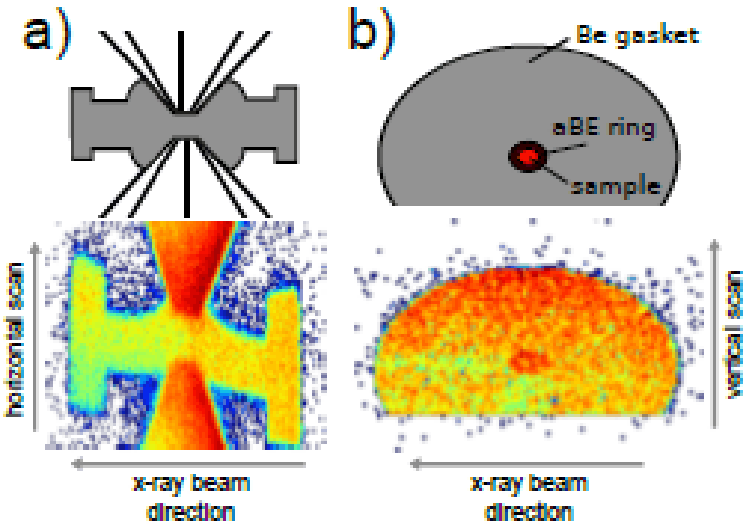

Figure 3.10: a) Horizontal sample scan where are clearly distinguishable the two regions of contrast from DAC compared to Be gasket; b) vertical alignment scan. These 2D images are useful when aligning the sample as the scale along the scanning direction is given by the absolute motor position of the instrument. The X-ray energy was set to the top of the elastic line at 9.7 keV (i.e. the contrast is given by S(q,0)). Image taken from Sahle[16].

response of the analyzer crystal; in this way the sample is aligned through the beam. After the alignment, at fixed position, the incident beam energy is scanned at steps of 0.25 eV and the scattered photons are collected at a constant energy $E_o = 9700$ eV. Inelastic features are found at $E_i - E_o \neq 0$ while at $E_i = E_o$ elastic scattering, with an intensity much higher than inelastic signal (several orders of magnitude), occurs. The elastic scattering is used, apart from evalueting the resolution as already mentioned, to gauge the absolute energy loss scale. When the scattered light is recorded by the pixels, to get the sample's spectrum only the pixels storing the scattered light from the very sample must be taken into account, all the other information (the scattering by the sample environment) must be discarded. This approach has the advantage of being applicable after the experiment has been performed.

Naturally, looking for instance at Figure 3.11, the question arises on how to select detector pixels associated with scattering from the sample as opposed to the sample environment. To do so, the scattering signal is analyzed with the XRStools software package (Sahle et al.[18]). There does not exist a unique method to do that, the most effective found for this specific case was the one that is now described (schematically represented in Figure 3.12 for a SiO_2 powder sample contained inside a Be high-pressure gasket): rough

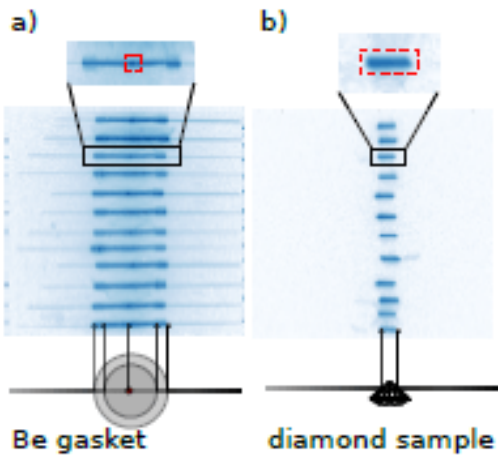

Figure 3.11: Typical detector images from the VU module for different samples. (a) Scattering form sample contained inside a DAC and (b) scattering from a diamond sample. The red dashed rectangles in the zoomed-in sections indicate possible choices for ROIs for the respective samples[17].

regions of interests (ROIs) are defined (ROI iteration 0 in Figure 3.12c)) by hand, then for each of the pixels inside these ROIs a spectrum is constructed and the intensity values of each spectrum as function of energy form a column of a matrix; 36 ROIs are thus defined, one per focus. Then, using the factorization scheme called "non-negative matrix factorization" (NNMF), the so formed matrix (where all the elements inside are non-negative) can be written as the product of two matrices with non-negative elements whose dimension can be much lower than those of the product matrix. In this way it is possible to obtain two matrices of reduced size, one representing the pixels where the searched spectral features coming from the sample are present, the other representing the ones where there is only a flat background coming from the sample environment (see Figure 3.12a)). The algorithm then calculates the covariance of the spectra from each of the pixels inside the rough ROI and those ones with a too low covariance can be discarded (Figure 3.12b), ending up with ROI iteration 1 in Figure 3.12c). In the last step each of the remaining pixels are analyzed one after the other and only one or two pixels per ROI where the clear sample spectrum is present are saved (ROI iteration 2).

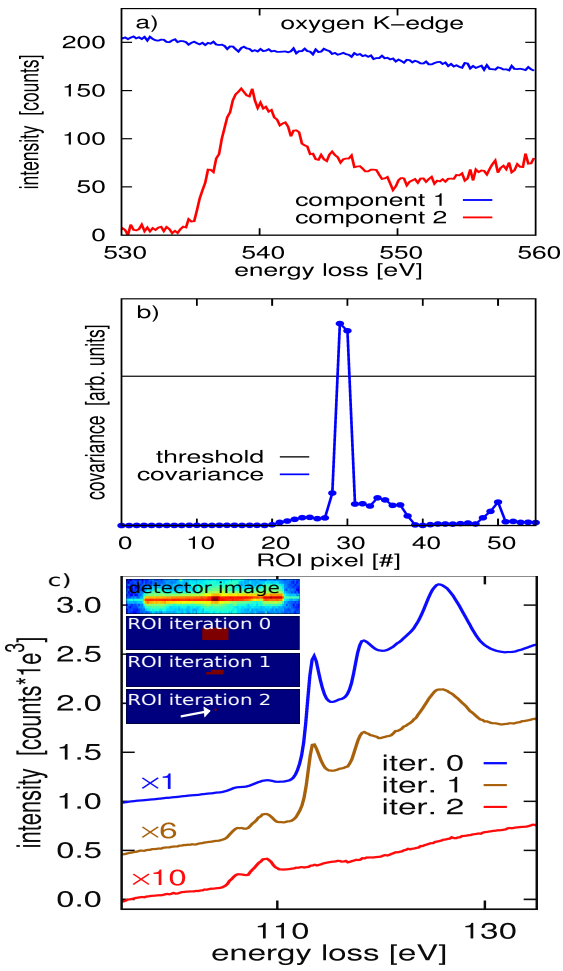

Figure 3.12: Example of ROI selection: (a) NNMF factorization scheme allows to separate the pixels containing only the background from the pixels containing the sample's spectral features. (b) covariance of the spectra versus ROI pixels. (c) ROI selection process: iteration 0, ROI selected by hand; iteration 1, ROI after NNMF factorization; iteration 2, ROI after pixel by pixel selection. Image taken from Sahle et al.[16].

Chapter 4

Sample and sample environment

4.1 The $K_2Mg(CO_3)_2$ system

In this thesis work the sample investigated was in a glass phase. Glasses are amorphous solids that lack long range order typical of crystalline structures. However, amid of the short range order present in perfect single crystal is preserved in the glassy state. Thus, unlike for the case of single crystal, it is not possible to define a translational operator. According to vibrational spectroscopic studies by Seifert[3], the glass phase is a good analogue of the melt phase that one would ideally want to study. Given the extreme difficulties to study samples at high pressure and high temperature, in a first step the investigation is conducted only at high pressures on the glassy phase.

Only few classes of carbonate melts are known to quench to carbonate glasses: one of these compounds, the one studied in this thesis, is the $K_2Mg(CO_3)_2$ system already studied by Genge and Jones via infrared and visible Raman scattering[2]. This compound is a double carbonate containing both alkalis and alkaline earth cations. The sample, used for the described investigation, was synthesized by Sylvan Petitgirad at the University of Bayreuth as follows[19]: polycrystalline powder of K_2CO_3 and $MgCO_3$ are mixed in equimolar proportions, kept at 383 K for 12 h to dry the compound and pressed into Au capsules. These capsules are placed in a cold seal hydrothermal pressure vessel and subjected to 0.1 GPa using CO_2 as pressure transmitting medium. Temperature is raised to 1023 K. Under these conditions the sample melts and if rapidly quenched to room conditions it yields a clear transparent glass.

$K_2Mg(CO_3)_2$ shows, as many glasses, three-dimensional rigid network structures representing random arrangements of interlinked polyhedra. The carbonate ionic group is, in theory, unable to polymerise forming long chains of CO bonds inside the structure it is placed in because all bonding orbitals

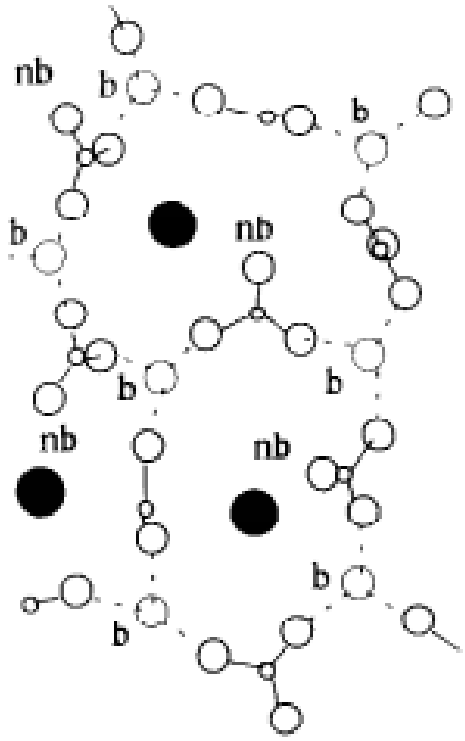

Figure 4.1: Schematic diagram showing carbonate framework structures. Straight lines are covalent bonds between C (small circle) and O (big circle); dashed lines are ionic bonds between O and Mg (light circle, labelled with "b" being the bridging cation); K, the network modifier represented by solid circles, is labelled with "nb" being the non-bridging cation. [Figure from Ref.[2]]

are already involved in intramolecular π- and σ-bonding and, hence, cannot form framework structures. However a random, three-dimensional framework structure could be made through ionic bonds between the carbonate groups and bridging metal cations; however, such a structure would not be rigid if this flexible arrangement of the carbonate glass is not supported by another metal cation specie acting as a network modifier. For this reason unary carbonates such as $MgCO_3$ do not quench to glasses, since no such modifiers are available to stabilise a glass framework structure. In our sample, thanks to the presence of both bridging and non-bridging cations, vitrification is possible and it yields the glassy $K_2Mg(CO_3)_2$ ring structure shown in Figure 4.1 found by Genge and Jones in their vibrational spectroscopic studies[2]. Thus, as reported in their studies, the main structure of this glass is formed by units of molecular metal-carbonate groups (Mg^{2+}) strongly interacting (by ionic bonds) with ${CO_3}^{2-}$, and the flexible metal-carbonate framework is supported by the network modifier specie (K^+) residing in in-

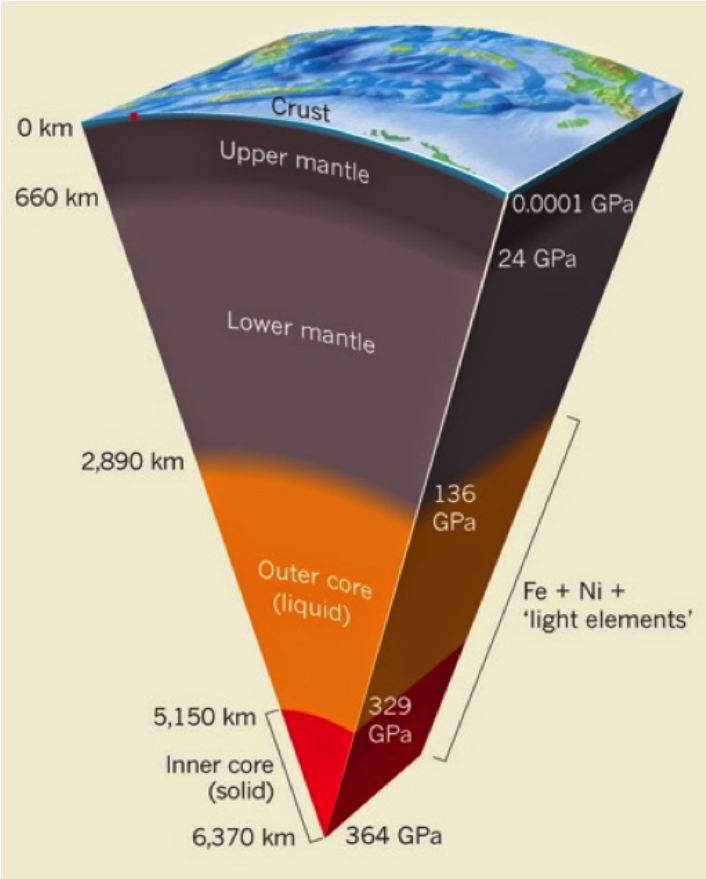

Figure 4.2: Cross section of the Earth showing the major layers, and the depths and pressures corresponding to their boundaries. Our pressures of interest go from the crust pressure up to the middle of lower mantle pressure. [Figure from Ref.[20]]

terstitial rings and weakly interacting (through Van der Waals force) with the CO_3^{2-} group. The occurrence of such large molecular metal-carbonate groups in the glass implies their presence in the melt phase (a reason why glasses are good analogues of melts according to Seifert and Mysen[3] as alraeady reported in Chapter 1), that are expected to be of such great importance in the control of the physical and chemical behaviour of the melt, thus critical to the petrogenesis of carbonatites, to the efficiency of carbonate melts as agent of mantle metasomatism in yielding deep carbon storage and to the diamond formation. The aim of the study is to see if applying pressures comparable to the ones present in Earth's lower mantle up to the expected transition occurrence, it is possible to observe a change in carbon's coordination from a tricarbonate to a tetracarbonate. A scale of pressures prevailing inside the earth is shown in Figure 4.2. This would represent, in

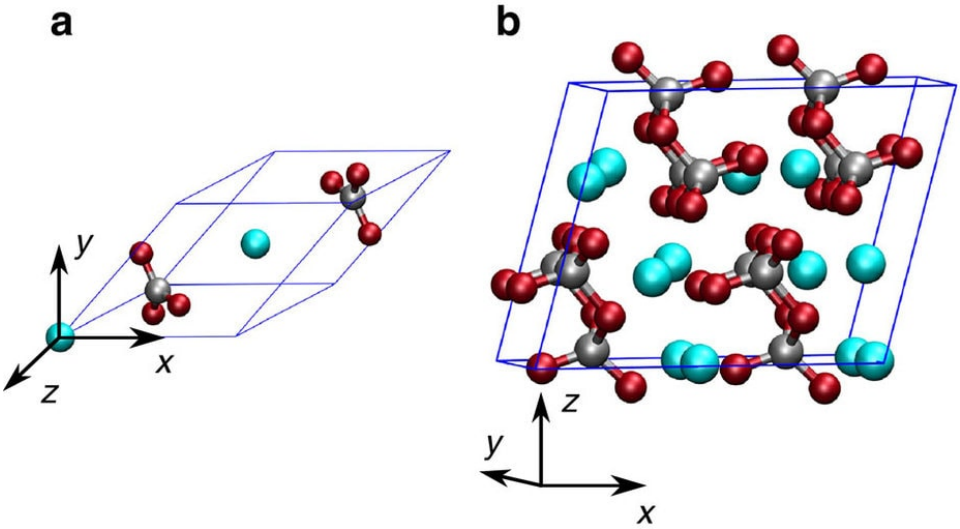

Figure 4.3: **a)** Ferromagnesite below 80 GPa. **b)** Ferromagnesite above 80 GPa where polymerizable network appears. Blue, red and grey spheres represent cation, oxygen and carbon atoms, respectively. [Figure from Boulard et al.[4]]

agreement with Jones and Genge[1], a step forward in the understanding of the solid reservoirs of carbon at deeper mantle pressures, in particular since experimental results suggest that the transformation could involve different carbon bearing phases, including nanodiamond formation[21]. If a transformation of melt structures to a tetrahedral carbonate occurs at lower mantle pressures, then a dramatic change in melt properties would be expected owing to the ability of $CO_4{}^{4-}$ to form polymerizable networks, as one can see in Figure 4.3. If the theoretically predicted increase in carbonate melt viscosity at high pressures are verified[1] this behaviour would fundamentally inhibit mobility of carbonate melts in the lower mantle. Significant changes in chemical and physical properties would mean change in their solubility for metal cations and in their reactivity; this change could be relevant for storage of deep mantle carbon and it could be foreseen precipitation of solid phases from rising carbonate melts. Then, to detect this transition the oxygen K-edge will be excited via X-ray Raman scattering (XRS), where changes in spectral features will be associated to changes in the carbonate glass structure. Due to the current difficulties of studying samples under simultaneous high temperature and high pressure conditions, necessary to form melts, $K_2Mg(CO_3)_2$ was studied only under high pressure conditions at ambient temperature, *i.e.* in the glassy state. At present, the use of glasses as analogues provides therefore the only experimental mean of studying carbonate melt structures under extreme pressure conditions. To generate high

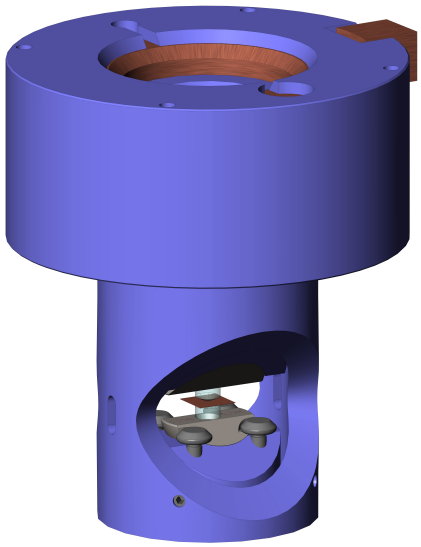

Figure 4.4: Sketch of a panoramic diamond anvil cell, as the one used in X-ray Raman spectroscopy in ID20. [Figure realized by Christian Henriquet].

pressure condition diamond anvil cells (DAC) were used, where the sample is placed in after having reduced it to a powder form, as described in the next chapter.

4.2 Sample environment: DAC

The diamond anvil cell (in the panoramic version in Figure 4.4, which is the one used in the experiments of this thesis) is a uniaxial stress device for high pressure generation, able to reach pressures beyond 300 GPa[22]. Single crystal diamond is generally used as the anvil material, due to its outstanding properties including: the highest known fracture toughness and hardness, the highest electron dispersion, high dielectric breakdown, radiation hardness, the highest thermal conductivity, very low friction and adhesion, ultra high melting temperature and chemical inertness[23]. The diamonds used have a height of 1.5 mm, a small face at the bottom of about 250 μm, the so called culet, on one end (the one facing the sample, see Figure 4.5), and a large base at the other end.

The applied force is loaded onto the large base of the two diamonds (Figure 4.5) through the pneumatic expansion of a membrane included in the cell and transmitted directly to the small culet facets, where the pressure is amplified according to the ratio of the two areas. The anvils sustain

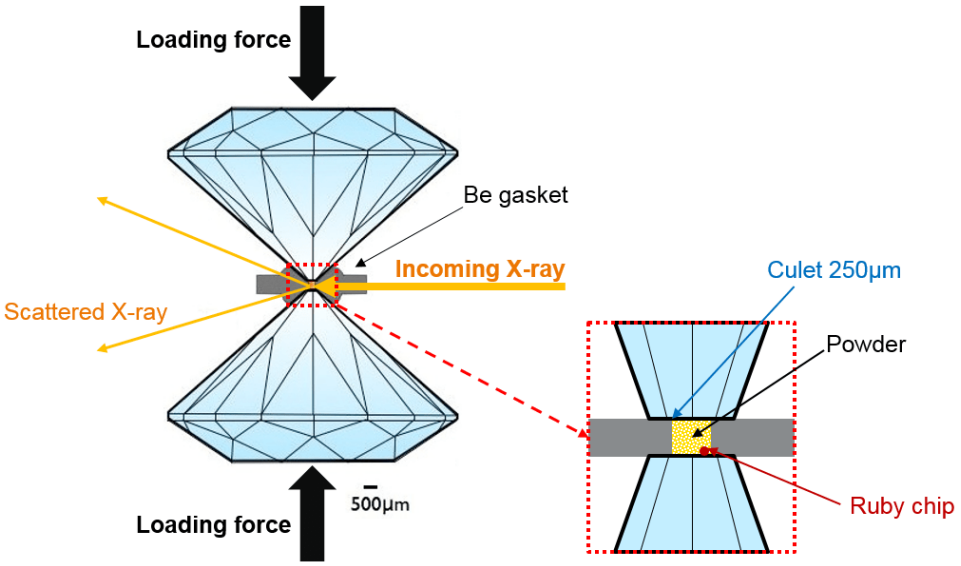

Figure 4.5: Structure of DAC in radial geometry, *i.e.* with the X-rays (in yellow) passing through the beryllium gasket; the black arrows represent the loading forces. In the red panel one can see the sample chamber made by the drilled gasket and the culet of the diamonds; the sample is put inside in a powder form together with a ruby chip to the exploitation of the ruby pressure gauge. Sketch realised by the author.

increasing pressures up to the strength limit of the diamond. At extreme condition elastic deformations can occur; with increasing deformations, small defects or strain might cause fractures in diamond. Thus, the quality of anvils is critical to reach extremely high pressures. Factors in selecting diamond anvils are: size, shape, birifrangence, optical transparency, orientation and fluorescence (Shen and Mao[23]). Since the diamond is highly absorbant of X-ray energies below 10 keV, a radial geometry was chosen (already shown in Figure 4.5), *i.e.* X-rays enter through the gasket perpendicularly to the compression axis, overcoming both geometric and absorption constraints of the conventional DAC. Using this geometry, a gasket that is permeable for X-rays, *i.e.* that has high transmission and yields low scattering background, is needed. Practically only beryllium can be used for this purpose, but, apart from being poisonous, it is also hard and brittle[24] and better materials from a mechanical point of view, like rhenium or stainless steel, could be chosen: however these materials are highly absorbing for X-rays in the 10 keV range. Therefore, beryllium is often used for experiments up to 100 GPa.

The gasket is an essential component serving as a sample chamber (thanks to the 100 μm hole drilled in its center by laser ablation), as a medium to support the pressure (because of the friction between the diamond anvil and

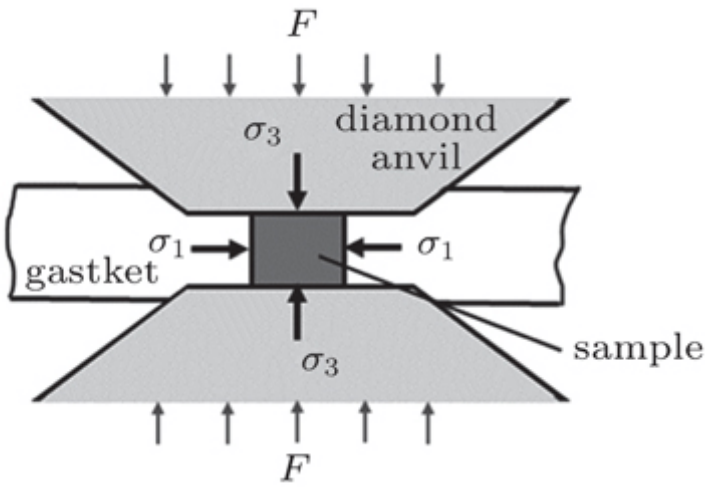

Figure 4.6: Stress state of the uniaxially compressed sample in a DAC, from Ref.[26].

the gasket itself) and, in this case, as the window for the X-rays. The effectiveness of the support depends on the tensile strength and thickness of the gasket. Between the two diamond culets the gasket sustains a large pressure gradient from the minimum stress at the edge of the culet to the maximum stress near the center. According to the lattice strain theory[25] the stress state of a sample in a DAC can be described by a maximum stress along the cell loading axis, σ_3, and a minimum stress in the radial direction, σ_1 as shown in Figure 4.6. The hydrostatic stress component is related to σ_3 and σ_1 by

$$\sigma_P = (\sigma_3 + 2\sigma_1)/3 \tag{4.1}$$

The difference between σ_3 and σ_1 is termed as the uniaxial stress component τ

$$\tau = \sigma_3 - \sigma_1 \tag{4.2}$$

The existence of the differential stress τ makes the sample in the DAC always subjected to a non-hydrostatic compression which can strongly affect the sample measured. To avoid this problem a so called pressure transmitting medium is usually used, which can be an inert gas, in order to provide hydrostatic pressure to the sample. In the current case no pressure transmitting medium was used as the glass sample was loaded in form of a powder, for which non-hydrostatic conditions are less of a concern due to powder averaging, that is checked in different points of the sample chamber to be sure that hydrostatic conditions are maintained. Gas loading is more crucial for the case of studying a single crystal sample, because in that case there is

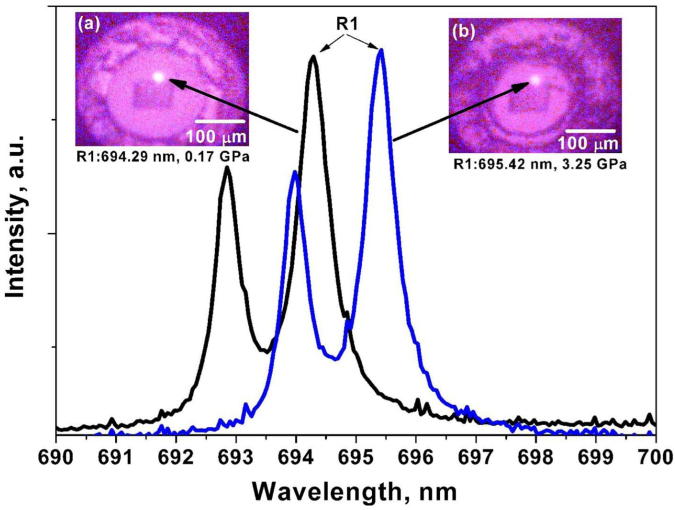

Figure 4.7: Intensity of ruby fluorescence vs. wavelength at two difference pressures within a DAC. Since the position of the peak maximum is very sensitive to the pressure, tha wavelength of the fluorescence line is a useful pressure scale. Figure from Rivers et al.[29].

only uniaxial pressure and direct contact between the sample and both the diamond culets simultaneously must be avoided to prevent diamond failure.

To measure the pressure inside the sample chamber an optical method is employed, using the wavelength shift of the ruby fluorescence line as described below. Three tiny ruby grains (between 5 and 10 μm size in diameter) are put in three different positions in the sample chamber and the pressure value around the ruby is measured thanks to the ruby fluorescence wavelength shift: a laser beam passing through the diamond excites the ruby and its fluorescence light is detected[27]. Since rubies contain Cr^{3+} ions surrounded by oxide ions, electronic transitions among the Cr^{3+} valence electrons produce a fluorescent emission at about 694 nm at room pressure[28]. When the ruby is under pressure, the oxide ions move closer to the Cr^{3+} ions systematically changing the electron energy levels and shifting the wavelength of the fluorescence line; thus, by shining a laser through a DAC onto a ruby crystal and measuring the shift of the main lines of the ruby fluorescence spectrum versus a standard (*i.e.* the position at ambient condition), it is possible to determine the pressure on it with an accuracy within 2% up to 55 GPa. An example of ruby fluorescence shift is shown in Figure 4.7.

Figure 4.8 shows a photograph of the used apparatus for the pressure calibration: a green guide laser is used to illuminate the sample in the DAC and locate the ruby chips profiting from a camera. The ruby fluorescence is then excited with a blue laser, whose wavelength is 458 nm, lighting up the pointed ruby chip and the radiated fluorescence is then analyzed by a

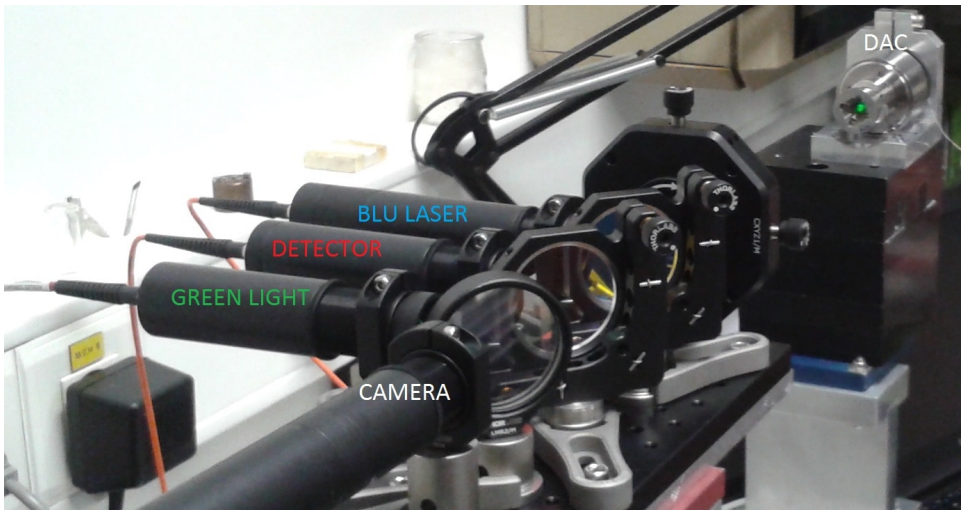

Figure 4.8: Ruby pressure gauge laser setup.

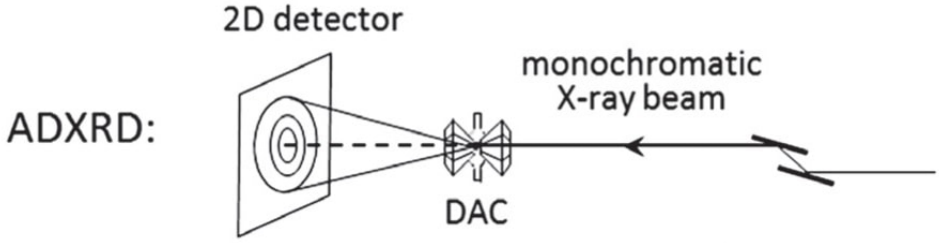

Figure 4.9: ADXRD sketch, figure from[26].

spectrometer (in red in Figure 4.8). The fluorescence spectrum so obtained is then shown on a monitor in order to check the actual pressure on the ruby reading the position of the maxima and using the *Kantor* software[30] to estimate pressure. Measuring the pressure in different positions can provide information on the hydrostaticity in the sample chamber.

The sample filled into the DAC in a fine powder form is made by grinding it using an agate mortar, then the diamonds are squeezed in order to confine it in the sample chamber. To verify that the $K_2Mg(CO_3)_2$ sample inside the DAC is indeed in a glassy state, angle dispersive X-ray scattering was exploited at beam line ID15B at the ESRF. A typical XRD setup is shown in Figure 4.9. To allow powder diffraction in XRD configuration the polychromatic X-rays from an in-vacuum U20 insertion-device are focused by vertical and horizontal transfocators and are monochromatized at 30 keV by a Si (111) monochromator; then they impinge upon the sample. The exposure time used was 1 second. The diffraction patterns are recorded using a Mar555 image-plate detector, which has an active area of 430x350

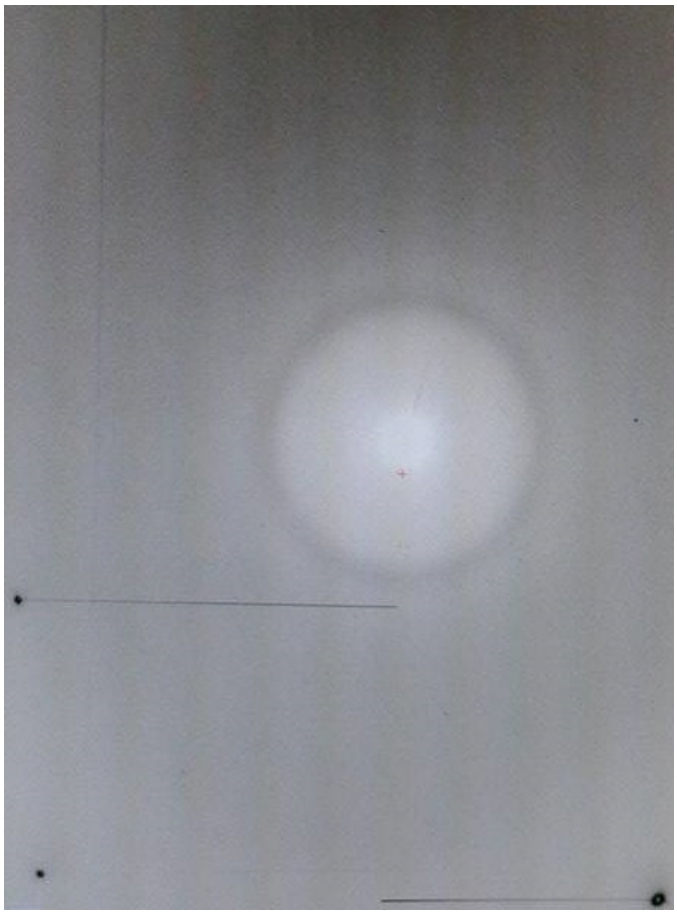

Figure 4.10: Diffraction pattern of the sample inside the DAC.

mm^2 [26]. The energy of the X-ray is fixed, the sample-detector distance is about 30 cm, in order to collect all the light from the DAC opening angle. Figure 4.10 shows the raw detector image, Figure 4.11 the azimuthally integrated intensity versus the scattering angle 2Θ. In the former figure a halo pattern is clearly recognizable, which is a fingerprint of the short range order described in chapter 4.1 and typical of all the amorphous materials (Ref. from Ossi, *Disordered materials: an introduction* [31]), while the black spots arise from Bragg diffraction of the diamond anvils; in the latter we observe the presence of a large bump distributed in a wide range of the scattering angles instead of high intensity narrower peaks, due indeed by the random distribution of atoms in 3D space. After two days of XRS experiments on ID20, XRD experiment was repeated on ID15B in order to verify that the sample's glassy form was preserved; it was observed that the amorphous form was maintained.

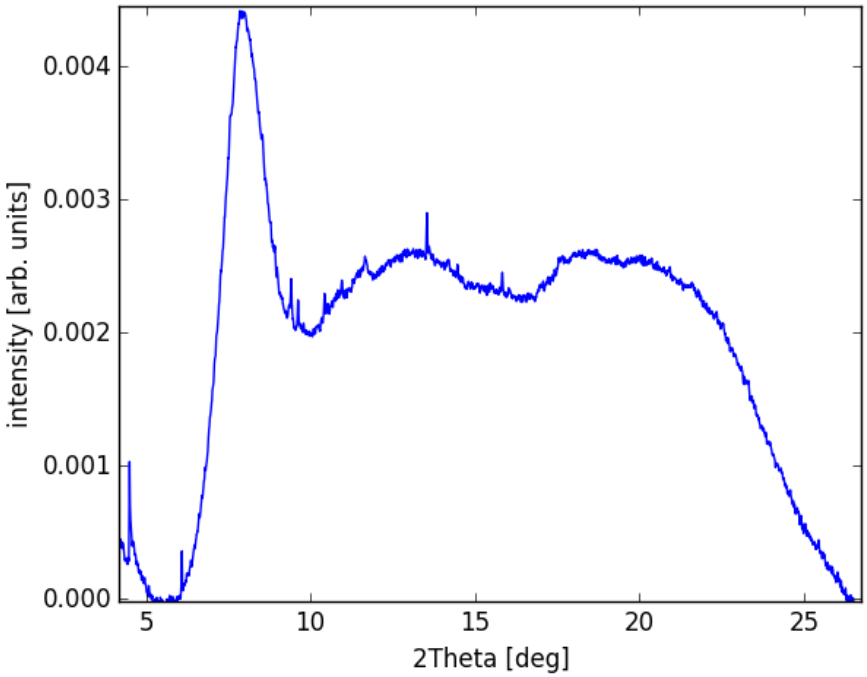

Figure 4.11: Diffraction spectrum of the sample.

Chapter 5

Results

In this chapter the XRS spectra of the glass powder $K_2Mg(CO_3)_2$ at different pressure points are reported and analyzed. The scattered radiation was collected in the vertical scattering plane by three analyzer chambers (as already described in Chapter 3.2.1), the only ones accessible when using the panoramic DAC (diamond anvil cell). Since this work is focused on the carbonate group behavior and because of the background that could be introduced by the diamond environment, the experiments were performed observing the oxygen K edge by varying the incident energy in order to cover the energy loss range from 520 to 555 eV in steps of 0.2 eV of 10 seconds each. In this way one scan is acquired: usually several scans are acquired, checked for consistency, and summed together in order to improve the signal to noise ratio. However, significant variation amongst the single scans prevented from averaging over them. These time dependent changes were assigned to radiation induced alterations of the sample as described in section 5.1 of this Chapter. Here, the spectral changes induced by the X-ray beam are analyzed in detail in order to uncover cause and effect of this beam induced damage and define conditions for future experiments without these alterations caused by the X-ray probe. In section 5.2 the collected data are shown and studied in order to discover if systematic changes and structural variations exist.

5.1 XRS spectra of beam damaged sample

Figure 5.1 shows spectra collected at a pressure of $p = 5$ GPa for different exposure times. Strong spectral changes in the energy loss region of 530.0 - 533.0 eV can be observed, where a peak emerges that increases in intensity with increasing exposure to X-rays. This peak was observed at most pressure points measured after X-ray beam exposure of more than one hour. As confirmed by XRD, this peak is not related to a crystallization of the sample. In order to estimate the amplitudes of this peak as a function

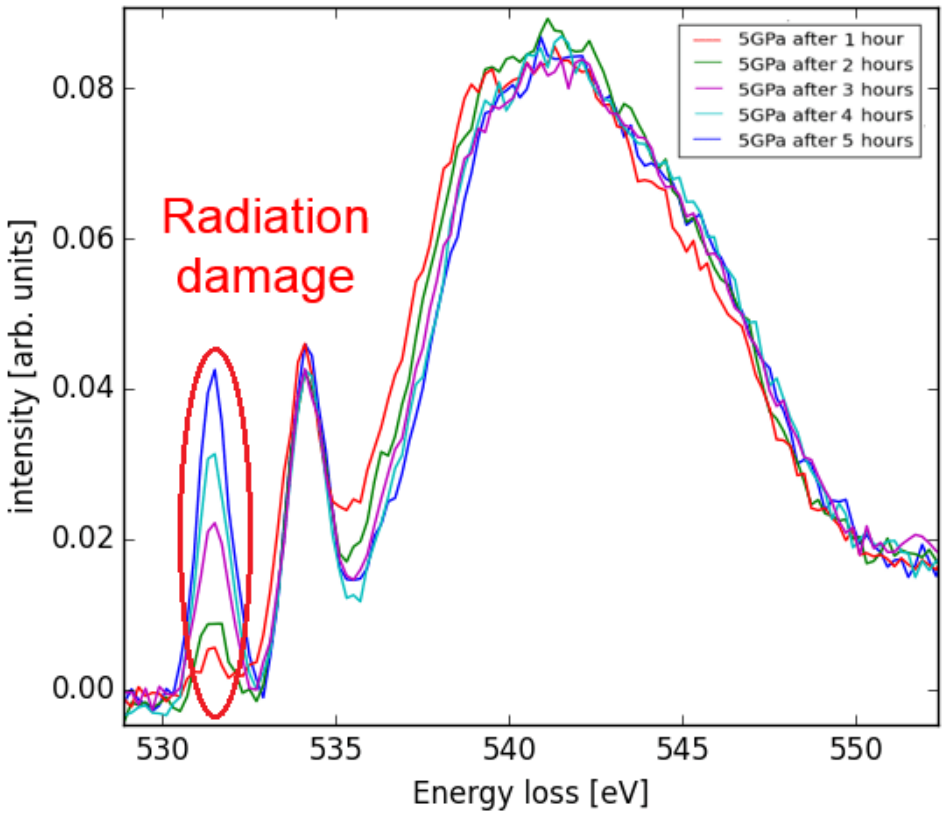

Figure 5.1: Spectra obtained at 5 GPa during 5 hours of acquisition, hour by hour; in the red circle is highlighted a spectral feature that could be associated with a radiation damage, the rising of a new peak at about 532 eV.

of exposure time, this peak is fitted with a Gaussian function given by the general expression

$$f(x) = ae^{-(x-b)^2/c^2}. \tag{5.1}$$

Thus, the estimated amplitudes are shown in Figure 5.2. The green line represents a linear fit among these points revealing a linear increasing behavior; extrapolating this linear fit to zero intensity, the amplitude value of the radiation damage is zero in correspondence of 30 minutes of exposition. This implies that exposure times up to 30 minutes would avoid radiation damage. However, it was found that after one hour of exposition the amplitude of this peak at about 531 eV is generally of the same order of magnitude as the background noise, *i.e.* the amplitude of the oscillations in the tail just before the peak. For this reason only signals collected after one hour of exposition

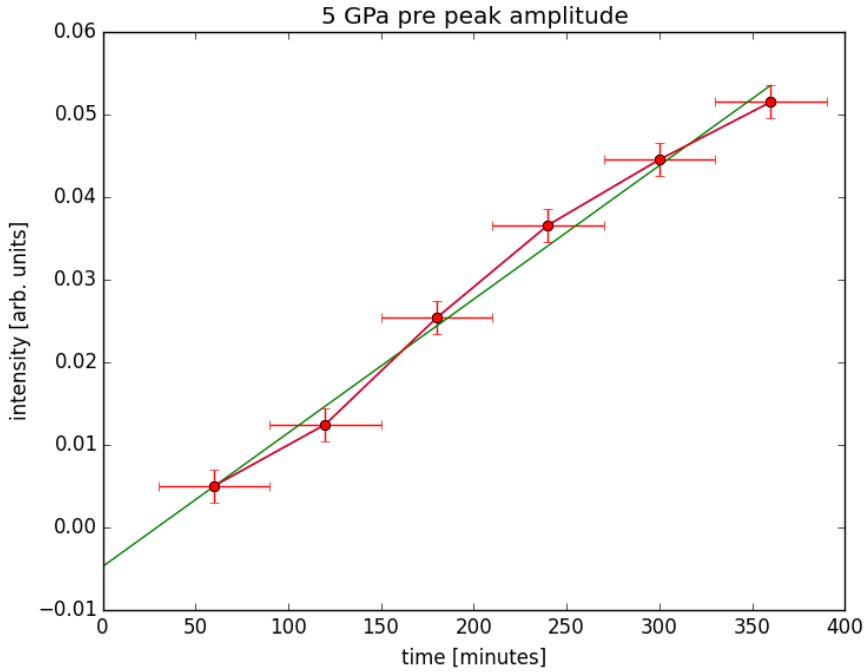

Figure 5.2: 532 eV peak amplitudes as function of time at 5 GPa. Experimental data in red, linear fit in green.

were chosen to be studied.

The mechanism of the beam damage is not entirely understood, it may occur for different processes of light-matter interaction, for example through absorption, secondary bond breaking, radical formation, fragmentation and aggregation[32], and it is not simple to interpret and to understand from spectroscopic data which are the causes that underline this effect. In an attempt to understand this additional peak in the oxygen K-edge spectrum, the measured data were compared with spectra of possible products formed during X-ray beam exposure. It was found that, amongst all the possible products that could form from the elements present in the sample ($MgCO_3$, K_2CO_3, CO_2, CO, O_2, O), only the spectrum of molecule O_2 fitted well the data. A spectrum of O_2 obtained from the Hitchcock database of the McMaster University[33] is shown in Figure 5.3. The new feature appearing in the glass looks to fit well the peak observed in the spectrum of molecular O_2. Thus, it is possible to speculate that the X-rays may fragment a portion of the oxygen present in our compound allowing them to recombine among themselves as O_2 molecules; with increasing X-ray exposure time, more O_2 is produced leading to an increase of the peak observed at 531 eV.

What can be concluded is that one hour of exposition is a good trade off

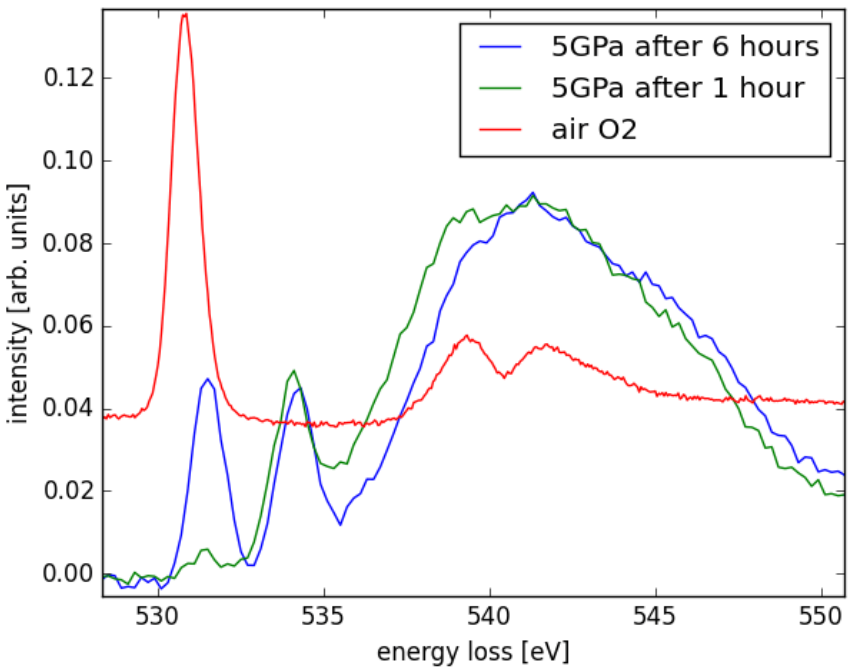

Figure 5.3: O2 spectrum in red compared with $K_2Mg(CO_3)_2$ spectra at 5 GPa after 1 hour (in green) and 6 hours (in blu) of exposition, respectively.

between the minimization of the beam damage effect and the collection of a signal with a good signal-to-noise ratio for the purposes of our study among all the pressures studied so far.

5.2 XRS spectra of $K_2Mg(CO_3)_2$

An example of a broad overview spectrum of the sample at a pressure of $p = 5$ GPa and for different momentum transfer is presented in Figure 5.4. The edge onsets of the elements constituting the compound studied and the sample environment (the latter formed by the gasket and the diamonds) are highlighted.

To investigate if a transition from ${CO_3}^{2-}$ to ${CO_4}^{4-}$ at high pressure, analogous to such a transition in the crystal, occurs, the carbon K-edge (in green in Figure 5.4) and the oxygen K-edge (in red in Figure 5.4), meaning the transition of the 1s electron into an unoccupied states (p-like states under the dipole approximation), are good candidates to be studied. Given the fact that the sample is surrounded by the diamonds (*i.e.* carbon atoms) the carbon signal could be corrupted, thus only the oxygen K-edge was chosen to be studied in detail. Moreover, despite the fact that the overall shape of

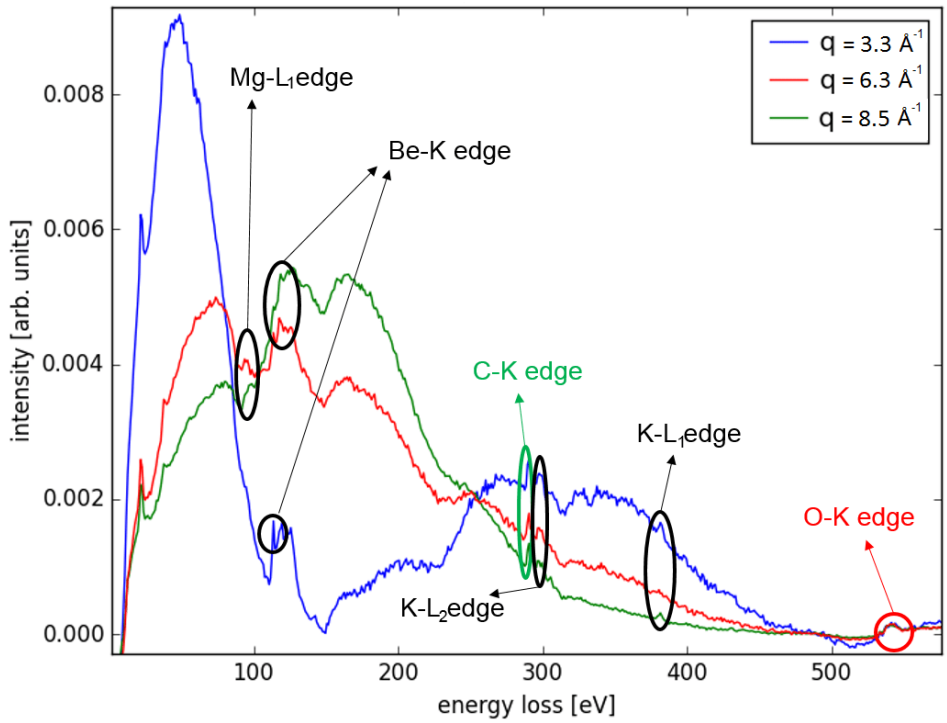

Figure 5.4: X-ray Raman scattering spectra of $K_2Mg(CO_3)_2$ at different momentum transfer (see the momenta values at Chapter 3.2.1) at 5 GPa versus energy loss from 5 eV to 605 eV. The different absorption edges involved are highlighted. The oxygen K-edge is red coloured.

the overview scan appears very sensitive to the momentum transfer, the O K-edge shows very little momentum transfer dependence. Thus, the signals collected for the different momentum transfers are summed up. Figure 5.5 shows the spectra collected within one hour of exposure to the X-rays (see Chapter 5.1). The spectra shown in this figure thus represent an average signal of the first two out of a number of scans, varying from seven to fourteen, taken per pressure points. Signals from all 36 analyzer crystals were likewise averaged. The maximum pressure reached in this way was 29 GPa, *i.e.* well below pressures corresponding to those prevalent at the core-mantle boundary of the inner Earth. Turning back to the data collected, in Figure 5.5 the most relevant spectra extracted are shown, presenting the O K-edge of the sample at 5, 7.6, 10.6, 16.6 and 28.8 GPa. The statistical accuracy of the data is poor, due to the fact that the data shown are collected with an exposure time that is between $\frac{1}{5}$ and $\frac{1}{7}$ of the intended one. Moreover the background subtraction with this scarce statistic is a challenging task and a few data points exhibit negative intensity in the pre-edge region between

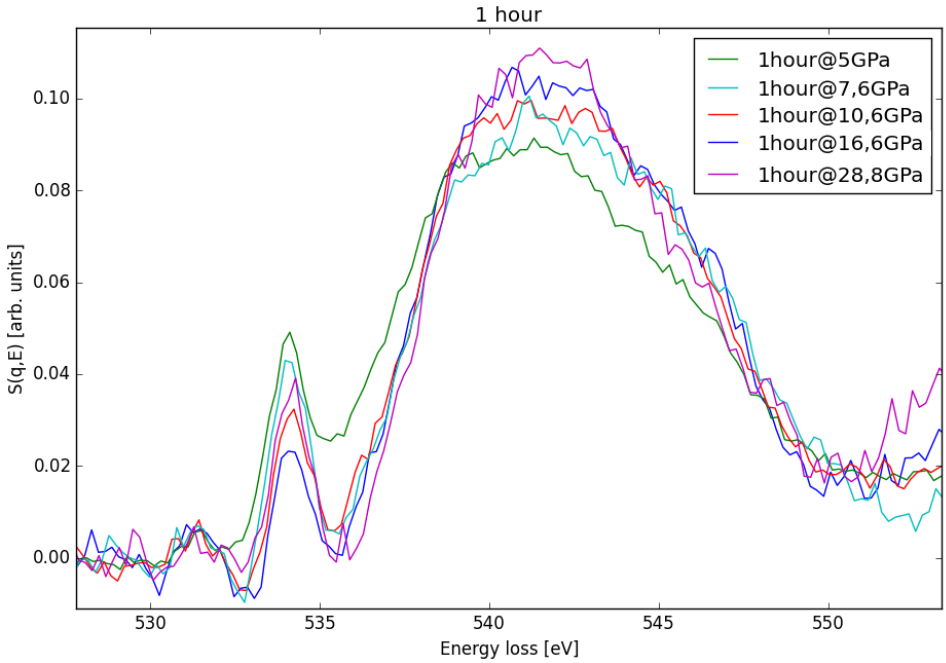

Figure 5.5: Spectra obtained after one hour of acquisition at different pressures from 5 GPa up to 29 GPa.

525 eV and 533 eV. These data may still be used, but results should be handled with care. First of all at 532 eV a small peak is visible, *i.e.* remnants of the beam damages described in Chapter 5.1, that anyway can be omitted for the reasons already explained. Then two bigger resonances are clearly visible: one at about 534 eV and the second one, much broader, centered around 542 eV. According to NEXAFS spectra and literature on carbonate ion systems[34], they correspond to the excitation of an 1s electron to a molecular π^* and σ^* state respectively. π and σ molecular orbitals of CO_3 ion are shown in Figure 5.6.

In the case of σ^* the origin of this broad feature (with FWHM at around 9 eV) is not very well understood: it could result from a splitting of molecular σ^* states or a shape resonance due to the interaction with the bridging cation. As pointed out by Madix and Solomon[34], the σ^* resonances are sensitive to the bond length, providing a direct measure of the CO distance. The π^* resonance is, instead, sensitive to the OCO angle variation. Moreover, looking at studies conducted by Hesse and Simons[19], it is possible to assert that the distance between carbon and oxygen atoms in the compound and the geometrical structure is similar to the corresponding crystalline phase. This assumption is reasonable due to the fact that, in spite of the breaking of long range order in the glass, the short range order (SRO) is maintained in the glassy phase implying that the CO distance and the structure are not

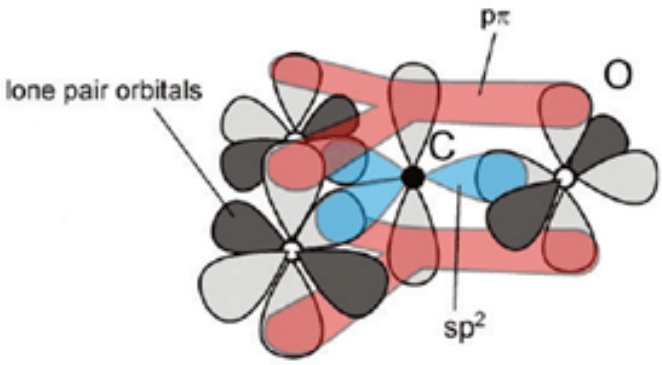

Figure 5.6: Molecular orbitals and electronic configuration of CO_3. Picture from Ref.[1].

that different than in the crystal. So it can be instructive to compare the behavior of the crystalline form of the sample, studied by Gulobkova and Merlini[35], with the features of the spectra obtained at increasing pressures. To understand better the characteristics of the curves collected, the π^* and the σ^* features were fitted with Gaussian functions as already done in the previous chapter. After having recovered from the fit all the Gaussian parameters, important properties for the curves, such as amplitudes, center positions and FWHMs are found. After obtaining the parameters, they are plotted together to find out if information about the compound at increasing pressures can be extracted and if systematic variations exist. In Figure 5.7 the amplitudes, center positions and FWHMs of the pre edge peak, i.e. the π^* resonance, are shown. The pressure error bars are 1 GPa long for all the pressures but 2.9 GPa long for 26.9 GPa. This is because at this pressure point the system lost pressure during the acquisition, and the value reported is the one in the middle between the initial and the final value $\pm$ 2.9 GPa. The intensity error bar is taken by the amplitude of the background noise, *i.e.* the intensity magnitude of the tail before the peak; the energy error bar is given by the energy distance at which two different peaks can be solved and this energy distance is demonstrated to be at around 0.4 eV. As one can observe in the graphics of Figure 5.7 the amplitudes and FWHM values look to have a systematic linearly decreasing behavior up to 16.6 GPa; then both intensity and FWHM increase at 26.9 GPa. It is not obvious how to interpret this behaviour: at 26.9 GPa it is possible that the intensity increases because, as suggested by Westre and al.[36], some π orbitals could mix with other carbon orbitals as the bond length decreases, increasing again the transition probability. This is a possibility that only an accurate theoretical model, for instance a model based on molecular dynamics simulations, could clarify. The behavior of the center position of the peak is more stable, with

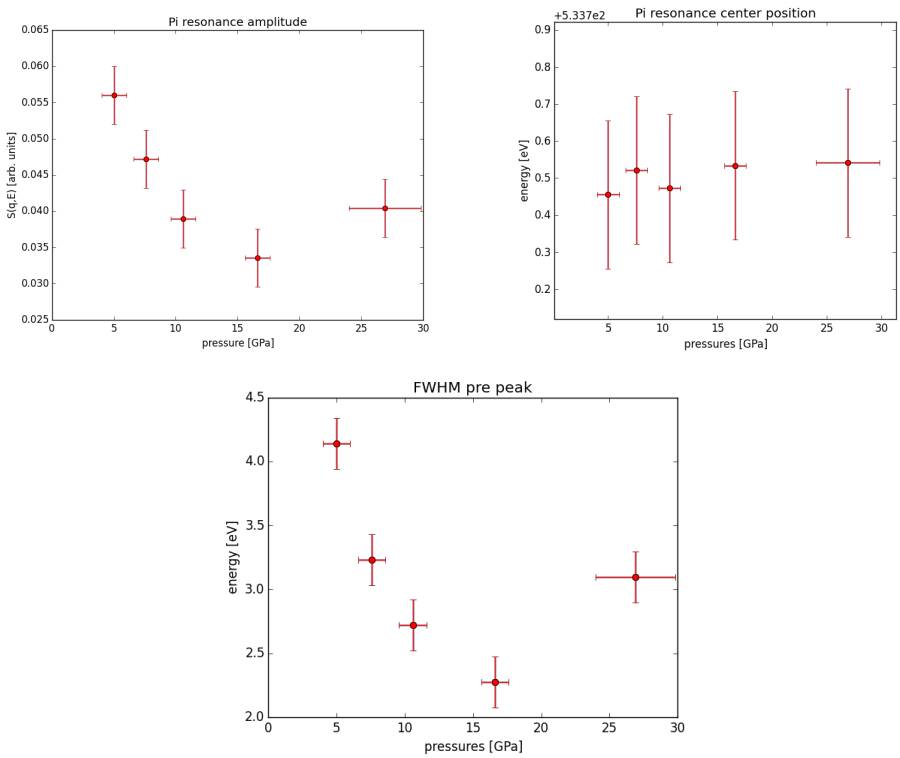

Figure 5.7: Pre peak data. From top left to bottom right: amplitude of the peaks (intensity vs pressure); center positions of the peaks (energy vs pressure); FWHMs (energy vs pressure).

an average value at about 534.2 eV: this means that for the π^* resonance no relevant energy shift at increasing pressures is present. In Figure 5.8 the data referred to the σ^* resonance are shown. Here the behavior of the amplitudes and the FWHMs are reversed, increasing in the first case and decreasing in the second, and more systematic, in fact 26.9 GPa does not deviate from the trend. But the main difference stands for the center positions of the peaks which, instead of being constant like in the previous case, they slightly shift to higher energy: this can be related directly to a change in the bond length, as observed by Madix and Solomon[34], in particular a decrease of the bond length; indeed after an increase of the pressure, a decrease of the bond length and a shift to higher energies for the charge superposition is expected. In this respect, the intensity trend for the σ^* resonance looks coherent with this picture, meaning that the lower the bond length the higher the superposition between the orbitals, hence the higher is the bond covalency and finally the intensity. So far conclusions related to the length of the CO bonds were drawn, but nothing is said about the local structure of the carbonate: to have a further insight, Figure 5.9 shows how the biggest changes in the

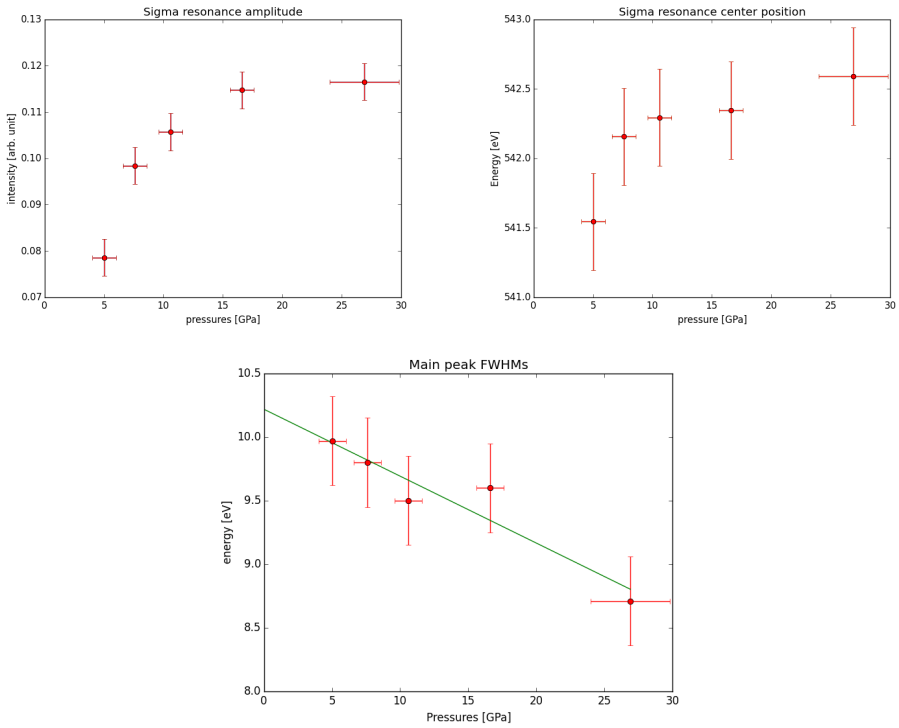

Figure 5.8: σ^* data. Top left: amplitude of the peaks (intensity vs pressure); top right: center positions of the peaks (energy vs pressure); bottom: FWHMs with linear fit in green (energy vs pressure).

spectra occur passing from 5 Gpa to 7.6 GPa. This has no simple interpretation; however, looking at studies on the crystalline form of $K_2Mg(CO_3)_2$ by Golubkova[35] at high pressure, a plausible answer can be provided. The crystalline structure is shown in Figure 5.10 which basically has the same picture of the glass (Figure 4.1), but, of course, also exhibiting long range order. It is also known from Golubkova[35] that at 8 GPa the crystal transforms from a rhombohedral initial geometry into a monoclinic one accompanied with 1% density increase, as is shown schematically in Figure 5.11. Thus it exists the possibility that the change in the spectra is somehow correlated to a geometry change that could be similar to the one occurring in the crystal. Two facts support our conclusion: the pressure at which this variation is observed is very close to the one discovered by Golubkova and the energy shift and amplitude variation of σ^* resonance is much higher passing from 5 GPa to 7.6 GPa than passing to all the others pressure points meaning that this could happen because the geometry change makes the compound denser abruptly reducing the CO bond length.

Therefore it can be concluded that structural similarities between the

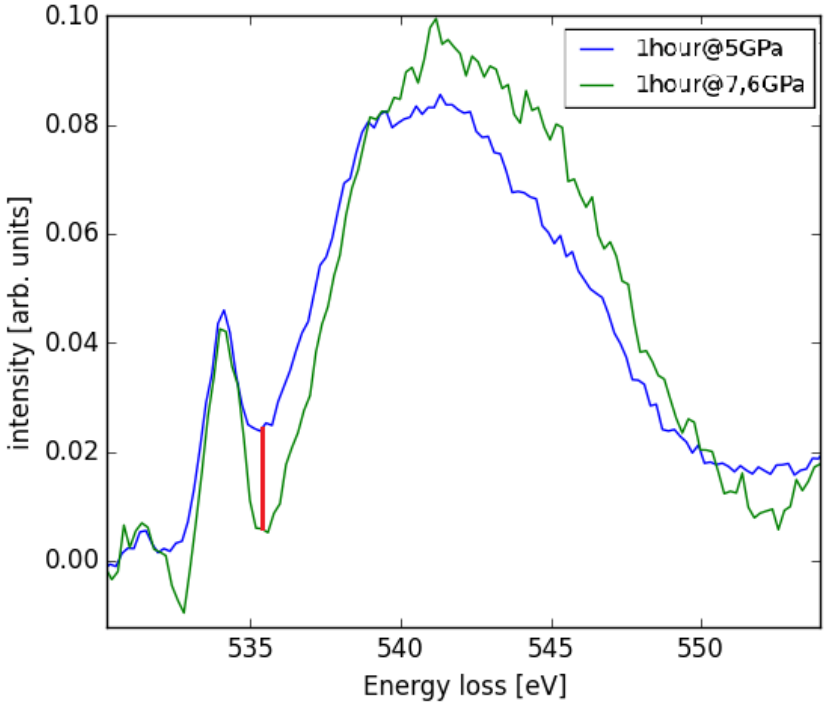

Figure 5.9: 5 and 7.6 GPa spectra after one hour of acquisition with, in red, the jump at about 535 eV.

crystalline and the glassy phase exist up to 29 GPa and there could be instructive to study the two phases in parallel to investigate for relations and deviations among them at increasing pressure.

In summary, the presented data defy conclusions about a possible structural and electronic transition from CO_3 to CO_4. However, important aspects were drawn nevertheless.

Firstly, there is now a good strategy for the future on how to successfully perform the experiment. The beam damage will be taken into account in order to find the best condition of exposure time and calibrate all the successive runs. The beryllium gasket will be substituted with a rhenium one, having the property to be ductile, to have big bulk and shear moduli, a high strength and a high melting point[37]. This makes rhenium the best and the most stable metal for DAC's gasket from a mechanical point of view, notwithstanding it absorbs X-rays much more than beryllium. To avoid this problem the geometry of the impinging X-rays will be modified, passing from the radial to the axial geometry (like the one seen for the diffraction in Figure 4.9), where, however, there was the problem of the absorption of the X-rays by the diamonds. To overcome this problem, new 0.5 mm high

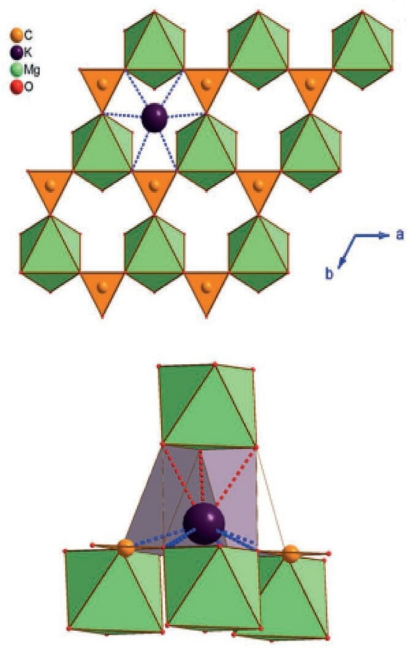

Figure 5.10: $K_2Mg(CO_3)_2$ low pressure crystal structure.

diamonds (instead of the 1.5 mm used) are under design in order to be used in a new DAC for the next experiments allowing to reduce the absorption by one third. So repeating this experiment in future with a different diamond anvil cell using a rhenium gasket and the newly designed short diamonds, good signals as the ones in this experiment or even better will be taken, but with more pressure stability and running the experiments faster.

Secondly, results of the current experiment, the spectra of $K_2Mg(CO_3)_2$ glass from 5 to 29 GPa, show the sensitivity of XRS technique to details of the local and electronic structure.

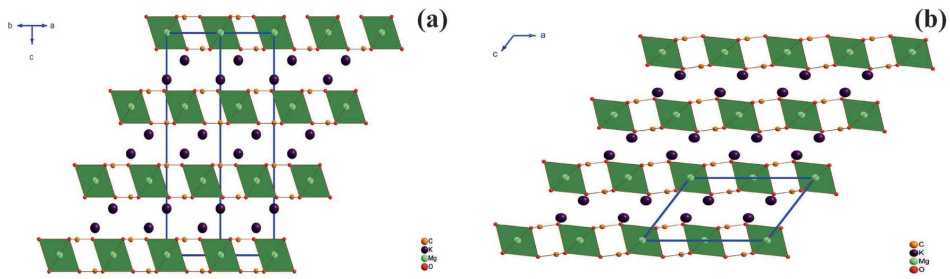

Figure 5.11: **a)** Structure of low pressure rhombohedral $K_2Mg(CO_3)_2$ (viewed along [110] direction) and **b)** monoclinic $K_2Mg(CO_3)_2$ at pressures above 8 GPa (viewed along [010 direction]). Picture by Golubkova[35].

Chapter 6

Summary and outlook

This thesis describes a first attempt at investigating the "tetracarbonate" transition in an amorphous carbonate material, which is of extreme relevance in the understanding of the carbon reservoirs at lower mantle pressures as noted by Oganov[38], using X-ray Raman scattering. If this transition exists, then CO_4 could form ploymerizable networks leading to significant changes in chemical properties and a drastic change in metal cation solubility; this would be extremely crucial for the understanding of the deep carbon storage. For the determination of this transition, the potential of the diamond anvil cell to generate high-pressure conditions, relevant to the ones prevailing in the mantle of our planet, and the spectroscopic technique of XRS (with the capability of providing X-ray absorption spectroscopy information under the extreme environment the sample is exposed to, with the property of being bulk sensitive and a self-absorption free probe of electronic structure of light elements) were combined together. Thus, the O K-edge of a prototypic sample, one of the few carbonate compounds that are quenchable to a glass, was studied: the glass phase of matter has the characteristic of being a good analogue for the melt. The maximum pressure reached was 29.8 GPa therefore rendering conclusions about any transition to a tetracarbonate impossible.

Nevertheless, systematic changes were observed as a function of exposition time and pressure giving a structural and compositional insight of the system and possible explanation on the evolution of the sample; this demonstrates the sensitivity of XRS to variations in local structure. But most importantly, there is now a clear strategy on how to manage the experiment in the future in order to conduct a successful experiment.

Figure 6.1 shows a sketch of the new diamond anvil cell (DAC) geometry that will be used for future experiments: the 1.5 mm high diamonds will be replaced with newly designed 0.5 mm high ones, which will allow to switch from a radial to an axial geometry thanks to the cut of one third of absorption that will be obtained by passing through the diamonds. In this way

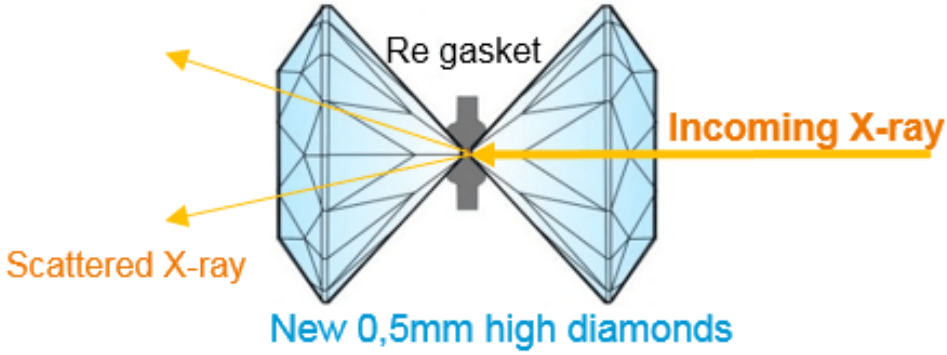

Figure 6.1: New DAC for the future XRS experiments with new designed diamond and exploiting axial geometry for the incoming X-ray. Rhenium gasket will guarantee more pressure stability.

there will be the possibility to replace the beryllium gasket with a rhenium one, which is the most stable material from a mechanical point of view for diamond anvil cell's gaskets[39] allowing to have more pressure stability and eventually experiments of better quality. With this new configuration the exposure time will be optimized in order to reduce the radiation damage, since it is known that this problem exists, so that precious time will be saved immediately dealing with it. For a better quality of the results it is also suggested to involve other techniques, *e.g.* XRD (X-ray diffraction) and PDF (pair distribution function), and the crystal phase of the sample in order to clarify the data obtained. Moreover, theoretical models and calculations can come in handy, for instance molecular dynamics in combination with spectrum calculations (*e.g.* by means of the *OCEAN* code, see Gilmore's paper[40]), to better understand what kind of transformation the system is undergoing. In a far future, after all these issues will be solved, it is possible to think to study the sample inside the DAC also at high temperature via laser heating, in order to study directly the melt phase, having in this way even a more similar condition to the actual one inside the Earth's mantle.

Bibliography

[1] Adrian P Jones, Matthew Genge, and Laura Carmody. Carbonate melts and carbonatites. *Rev Mineral Geochem*, 75(1):289–322, 2013.

[2] Matthew J Genge, Adrian P Jones, and G David Price. An infrared and raman study of carbonate glasses: implications for the structure of carbonatite magmas. *Geochimica et Cosmochimica Acta*, 59(5):927–937, 1995.

[3] Friedrich A Seifert, Bjorn O Mysen, and David Virgo. Structural similarity of glasses and melts relevant to petrological processes. *Geochimica et Cosmochimica Acta*, 45(10):1879–1884, 1981.

[4] Eglantine Boulard, Ding Pan, Giulia Galli, Zhenxian Liu, and Wendy L Mao. Tetrahedrally coordinated carbonates in earths lower mantle. *Nature communications*, 6, 2015.

[5] Rajdeep Dasgupta and Marc M Hirschmann. The deep carbon cycle and melting in earth's interior. *Earth and Planetary Science Letters*, 298(1):1–13, 2010.

[6] Simo Huotari, Tuomas Pylkkänen, Roberto Verbeni, Giulio Monaco, and Keijo Hämäläinen. Direct tomography with chemical-bond contrast. *Nat. Mater.*, 10:489–493, Jul 2011. doi: 10.1038/nmat3031. URL `http://dx.doi.org/10.1038/nmat3031`.

[7] Winfried Schülke. *Electron dynamics by inelastic X-ray scattering*. Number 7. Oxford University Press, 2007.

[8] JJ Rehr. Theory and calculations of x-ray spectra: Xas, xes, xrs, and nrixs. *Radiation Physics and Chemistry*, 75(11):1547–1558, 2006.

[9] Xiaosong Liu, Wanli Yang, and Zhi Liu. Recent progress on synchrotron-based in-situ soft x-ray spectroscopy for energy materials. *Advanced Materials*, 26(46):7710–7729, 2014.

[10] ESRF. What is a synchrotron?, 2013. URL `http://www.esrf.eu/about/synchrotron-science/synchrotron`. [Online; accessed on 19 December 2016].

[11] Brefeld Werner. Formulas: Accelerator physics and synchrotron radiation, 2016. URL `http://photon-science.desy.de/research/studentsteaching/sr_and_fel_basics/sr_basics/index_eng.html`. [Online; accessed on 19 December 2016].

[12] Id10eh1 overview, 2016. URL `http://www.esrf.eu/UsersAndScience/Experiments/SoftMatter/ID10/ID10EH1/BeamlineOverview`. [Online; accessed on 15 March 2017].

[13] Neil W Ashcroft and N David Mermin. Solid state physics (holt, rinehart and winston, new york, 1976). pages 490–495, 2005.

[14] Jens Als-Nielsen and Des McMorrow. *Elements of modern X-ray physics*. John Wiley & Sons, 2011.

[15] K Hämäläinen and S Manninen. Resonant and non-resonant inelastic x-ray scattering. *Journal of Physics: Condensed Matter*, 13(34):7539, 2001.

[16] Ch. J. Sahle, A. Rosa, M. Rossi, V. Cerantola, G. Spiekermann, S. Petitgirard, J. Jacobs, S. Huotari, M. Moretti Sala, and A. Mirone. Direct tomography imaging for inelastic x-ray scattering experiments at high pressure. *J. Synchrotron Radiat.*, 2016. In press.

[17] R. Verbeni L. Simoncelli A. Al-Zein K. Martel H. Gonzalez M. Moretti Sala S. Huotari M. Krisch G. Monaco Ch. J. Sahle, Ch. Henriquet. An x-ray raman scattering spectroscopy spectrometer at id20 of the esrf. October 24, 2016.

[18] Ch J Sahle, A Mirone, J Niskanen, J Inkinen, M Krisch, and S Huotari. Planning, performing and analyzing x-ray raman scattering experiments. *Journal of synchrotron radiation*, 22(2):400–409, 2015.

[19] K-F Hesse and B Simons. Crystal structure of synthetic k2mg (co3) 2. *Zeitschrift für Kristallographie-Crystalline Materials*, 161(1-4):289–292, 1982.

[20] Thomas S Duffy. Earth science: Probing the core's light elements. *Nature*, 479(7374):480–481, 2011.

[21] Eglantine Boulard, Alexandre Gloter, Alexandre Corgne, Daniele Antonangeli, Anne-Line Auzende, Jean-Philippe Perrillat, François Guyot, and Guillaume Fiquet. New host for carbon in the deep earth. *Proceedings of the National Academy of Sciences*, 108(13):5184–5187, 2011.

[22] J Li and Y Fei. Experimental constraints on core composition. *Treatise on Geochemistry*, 2:568, 2003.

[23] Guoyin Shen and Ho Kwang Mao. High-pressure studies with x-rays using diamond anvil cells. *Reports on Progress in Physics*, 80(1):016101, 2016.

[24] H Ahsbahs. Diamond-anvil high-pressure cell for improved single-crystal x-ray diffraction measurements. *Review of scientific instruments*, 55(1):99–102, 1984.

[25] Anil K Singh, C Balasingh, Ho-kwang Mao, Russell J Hemley, and Jinfu Shu. Analysis of lattice strains measured under nonhydrostatic pressure. *Journal of Applied physics*, 83(12):7567–7575, 1998.

[26] Liu Jing. High pressure x-ray diffraction techniques with synchrotron radiation. 2016.

[27] HK Mao, J-A Xu, and PM Bell. Calibration of the ruby pressure gauge to 800 kbar under quasi-hydrostatic conditions. *Journal of Geophysical Research: Solid Earth*, 91(B5):4673–4676, 1986.

[28] HK Mao, PM Bell, JW t Shaner, and DJ Steinberg. Specific volume measurements of cu, mo, pd, and ag and calibration of the ruby r 1 fluorescence pressure gauge from 0.06 to 1 mbar. *Journal of applied physics*, 49(6):3276–3283, 1978.

[29] Mark Rivers, Vitali B Prakapenka, Atsushi Kubo, Clayton Pullins, Christopher M Holl, and Steven D Jacobsen. The compres/gsecars gas-loading system for diamond anvil cells at the advanced photon source. *High Pressure Research*, 28(3):273–292, 2008.

[30] Fluorescence pressure calculation and thermocouple tools. URL `http://kantor.50webs.com/ruby.htm`. [Online; accessed on 17 March 2017].

[31] Paolo M. Ossi. *Disordered materials*. Number 2. Springer-Verlag Berlin Heidelberg, 2006.

[32] Jesse B Hopkins and Robert E Thorne. Quantifying radiation damage in biomolecular small-angle x-ray scattering. *Journal of applied crystallography*, 49(3), 2016.

[33] McMaster university. Gas phase core excitation database, 2005. URL `http://unicorn.mcmaster.ca/corex/cedb-title.html`. [Online; accessed on 12 December 2016].

[34] RJ Madix, JL Solomon, and J Stöhr. The orientation of the carbonate anion on ag (110). *Surface Science*, 197(3):L253–L259, 1988.

[35] Anastasia Golubkova, Marco Merlini, and Max W Schmidt. Crystal structure, high-pressure, and high-temperature behavior of carbonates

in the k2mg (co3) 2–na2mg (co3) 2 join. *American Mineralogist*, 100 (11-12):2458–2467, 2015.

[36] Tami E Westre, Pierre Kennepohl, Jane G DeWitt, Britt Hedman, Keith O Hodgson, and Edward I Solomon. A multiplet analysis of fe k-edge 1s 3d pre-edge features of iron complexes. *Journal of the American Chemical Society*, 119(27):6297–6314, 1997.

[37] Simone Anzellini, Agnès Dewaele, Florent Occelli, Paul Loubeyre, and Mohamed Mezouar. Equation of state of rhenium and application for ultra high pressure calibration. *Journal of Applied Physics*, 115(4): 043511, 2014.

[38] Artem R Oganov, Russell J Hemley, Robert M Hazen, and Adrian P Jones. Structure, bonding, and mineralogy of carbon at extreme conditions. *Rev Mineral Geochem*, 75(1):47–77, 2013.

[39] Elizabeth A Tanis, Hubertus Giefers, and Malcolm F Nicol. Novel rhenium gasket design for nuclear resonant inelastic x-ray scattering at high pressure. *Review of Scientific Instruments*, 79(2):023903, 2008.

[40] Keith Gilmore, John Vinson, Eric L Shirley, David Prendergast, C Das Pemmaraju, Joshua J Kas, Fernando D Vila, and John J Rehr. Efficient implementation of core-excitation bethe–salpeter equation calculations. *Computer Physics Communications*, 197:109–117, 2015.

Acknowledgements

This thesis is not a work of a single person, but of an incredible number of collaborating people without whom this thesis might not have been written that are gratefully acknowledged.

First of all thanks to Prof. Giacomo Ghiringhelli without whom this incredible experience would have been simply a far mirage.

A very special thank to Christoph Sahle, who followed me through all my work, teaching me how to deal with my job with patience and method, giving me precious advices and supervising the realisation of this thesis, being a friend before being a teacher.

Thanks to Chiara Cavallari, who helped me with gentleness in the beam line and gave me advices for my presentation.

A warm thanks to Matteo Rossi, PhD student at ID20, to have been literally beside me along these six months, helping me with kindness whenever I needed or I had any problem. I hope our friendship could go on.

Thanks to all ID20 staff: thanks to Marco Moretti, who represents a model to me and who decided to host me at ID20, for your supervision, your advices and your friendliness; thanks to Anna Efimenko, Christian Henriquet, Blanka Detlefs and Yi Yao.

Thanks to Valerio Cerantola, this project belongs more to him than to me, I humbly tried to bring a small contribute for the success of this research.

Thanks to Sylvain Petitgirard who prepared the sample in BGI, Bayreuth.

Thanks to my office mate Anuragh Kawde; a great thank you to my roommates and colleagues Andrea Carlantuono and Edoardo Cappelli, to share my life with you for six months was an instructive and funny experience.

Thanks to the city of Grenoble and to all the special people I have met there.

Thanks to my parents who always supported me through all my life in all my decisions never letting me alone; thanks to my brother who supported me discreetly but steadily.

Last but not least, thanks to Svitlana, the person who made this journey truly worthy enriching my life with love.

My deep gratitude to you all.